atmosphere

MDPI

Article

Vertical Accelerations and Convection Initiation in an Extreme Precipitation Event in the Western Arid Areas of Southern Xinjiang

Na Li [1,2,3,*], Lingkun Ran [2,*], Daoyong Yang [4], Baofeng Jiao [5], Cha Yang [4], Wenhao Hu [2], Qilong Sun [6] and Peng Tang [7]

1 China Meteorological Administration Hydro-Meteorology Key Laboratory, Beijing 100081, China
2 Institute of Atmospheric Physics, Chinese Academy of Sciences, Beijing 100029, China; huwenhao@mail.iap.ac.cn
3 Chongqing Meteorological Science Research Institute, Chongqing 400714, China
4 Xichang Satellite Launch Center, Xichang 615000, China; yangcha2011@163.com
5 School of Geomatics, Zhejiang University of Water Resources and Electric Power, Hangzhou 310018, China; jiaobf@zjweu.edu.cn
6 Chongqing Institute of Green and Intelligent Technology, Chinese Academy of Sciences, Chongqing 400714, China; sunqilong@cigit.ac.cn
7 Hotan Meteorological Bureau, Xinjiang 848000, China; aktpsx@163.com
* Correspondence: lina@mail.iap.ac.cn (N.L.); rlk@mail.iap.ac.cn (L.R.)

Abstract: A simulation of an extreme precipitation event in southern Xinjiang, which is the driest area in China, seizes the whole initiation process of the intense convective cell responsible for the high hourly rainfall amount. Considering the inner connection between convection and vertical motions, the characteristics and mechanisms of the vertical accelerations during this initial development of the deep convection are studied. It is shown that three key accelerations are responsible for the development from the nascent cumuli to a precipitating deep cumulonimbus, including sub-cloud boundary-layer acceleration, in-cloud deceleration, and cloud-top acceleration. By analyzing the right-hand terms of the vertical velocity equation in the framework of the WRF model, together with a diagnosed relation of perturbation pressure to perturbation potential temperature, perturbation-specific volume (or density), and moisture, the physical processes associated with the corresponding accelerations are revealed. It is found that sub-cloud acceleration is associated with three-dimensional divergence, indicating that the amount of upward transported air must be larger than that of horizontally convergent air. This is favorable for the persistent accumulation of water vapor into the accelerated area. In-cloud deceleration is caused by the intrusion or entrainment of mid-level cold air, which cools down the developing cloud and delays the deep convection formation. Cloud-top acceleration is responsible for the rapid upward extension of the cloud top, which is highly correlated with the convergence and upward transport of moisture.

Keywords: vertical velocity; convection initiation; southern Xinjiang; extreme precipitation

Citation: Li, N.; Ran, L.; Yang, D.; Jiao, B.; Yang, C.; Hu, W.; Sun, Q.; Tang, P. Vertical Accelerations and Convection Initiation in an Extreme Precipitation Event in the Western Arid Areas of Southern Xinjiang. *Atmosphere* **2024**, *15*, 1406. https://doi.org/10.3390/atmos15121406

Academic Editor: Anthony R. Lupo

Received: 30 August 2024
Revised: 6 October 2024
Accepted: 11 October 2024
Published: 22 November 2024

1. Introduction

Southern Xinjiang, which is the driest area in China, is experiencing an increase in extreme precipitation, making the accompanying flood disasters much more frequent than ever before [1,2]. Located in the south part of Xinjiang Province in China (Figure 1a), southern Xinjiang is characterized by very complex terrain with large mountains on three sides, the largest desert in China—Taklimakan Desert—and very unevenly distributed annual precipitation. The precipitation decreases from the west to the east and is mainly concentrated in the piedmont area between the desert and the high mountains [3]. In the long term, disastrous precipitation in southern Xinjiang has not been a big concern due to the arid environment and rare strong precipitation events [4]. However, historical records

show that once there is strong precipitation, serious floods occur more easily in arid areas due to the low vegetation coverage, the fragile ecological environment, and the influence of the snow-melting water from mountains [5]. This circumstance also occurs in other arid areas in the world, such as the recent floods in Pakistan from mid-June to August 2022, in the United Arab Emirates on 30 July 2022, and in the east of South Africa in April 2022. The increasing number of serious disasters indicates the urgent necessity for research on extreme precipitation in arid areas [6,7].

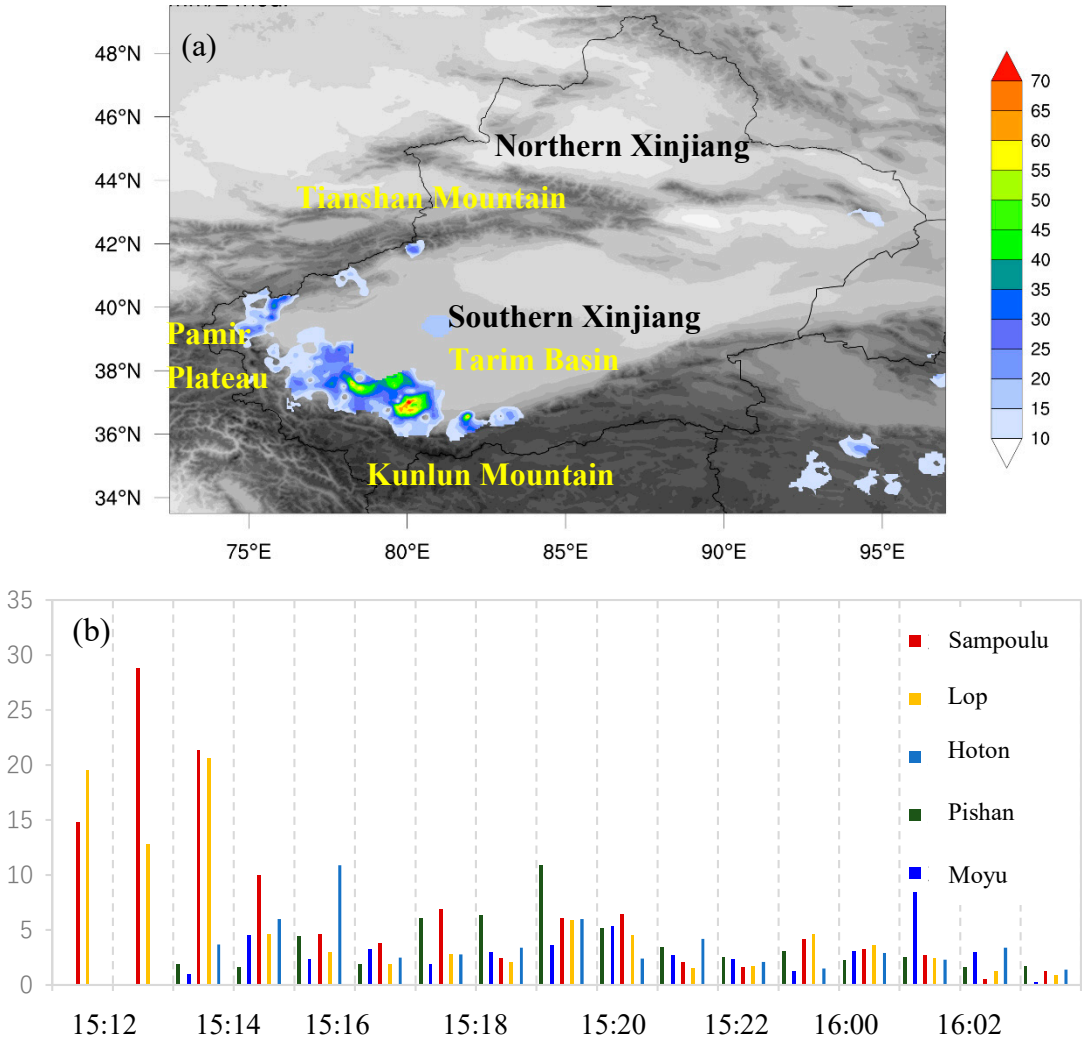

Figure 1. (**a**) Accumulated 24 h precipitation on 15 June 2021. (**b**) Bar chart of hourly precipitation over several automatic observation stations in southern Xinjiang.

Extensively large peak rain rates (hourly rainfall amount), which can sometimes be several times larger than the local annual precipitation amount, are an important feature of extreme precipitation in southern Xinjiang [8,9]. The city of Ruoqiang, which is one of the driest cities in southern Xinjiang, received 49 mm of precipitation in 6 h on 17 July 2005, which is approximately two times the local annual average precipitation amount. The recent extreme precipitation on 14–17 June 2021 which happened in Hotan in the west of southern Xinjiang had an hourly precipitation of 29.8 mm, which is nearly half of the local average annual precipitation amount [10]. When and where the extreme hourly precipitation tends to occur have thus become some of the most important questions needing to be solved to give a reliable early warning of disastrous rainstorm events.

Precipitation and convective clouds are intricately correlated. Cloud size, thickness, and lifetime, as well as the in-cloud liquid water content, microphysical processes, and

entrainment, have significant influences on rain intensity [11]. The positive feedback of cloud volume, larger updrafts, and higher liquid water content was regarded as a basic key process for strong precipitation formation. Considering the complex covariate relationship between rain intensity and convection, a fundamental task for the profound understanding of extreme precipitation is to discover how the associated convection is initiated and thereby how to predict the possible time and location of extreme rain rates in advance.

Convection initiation (CI) is also at present one of the most challenging subjects that have great impacts on severe weather predictions [12,13]. A central problem is the large uncertainty and limited predictability on the time and location of CI [14,15]. Basically, it is controlled by three factors, including moisture, instability, and lift, corresponding to the definition of deep convection initiation (DCI) [16,17]. However, in most cases, they are not sufficient for three major reasons. (1) CI is sensitive to minor changes in surface moisture and temperature, but the boundary-layer small-scale processes such as turbulence and horizontal convective rolls tend to disturb low-level moisture and temperature, especially over complex terrain and heterogeneous land surfaces; these processes are difficult to observe or accurately represent in numerical models [18–22]. (2) The entrainment, which is also hard to measure and parameterize, exerts significant influence on the nascent growth of cumuli [23]. (3) Microphysical processes in clouds are responsible for the positive buoyancy forming deep convections, but they are also complex and difficult to describe accurately and can be greatly influenced by, for example, the nucleus number and in-cloud turbulence [24,25]. Through decades of studies and large observation experiments, the improvement of CI predictions is still lagging.

Limited understandings and representations of the above unresolved physical processes are important reasons to resolve CIs. According to their effects on CI, they can roughly be divided into two categories: positive-effect processes and negative-effect processes. In most cases, when conducting a prediction, we tend to pay more attention to the positive effects, such as moisture convergence, frontogenetical lifting, and positive buoyancy by condensation latent heating [26,27]. The convective parameters that contribute positively to identify CI include convective available potential energy (CAPE), lifting index (LI), Severe Weather Threat (SWEAT) Index, etc. However, the importance of incorporating negative-effect processes, such as the entrainment of both surrounding and upper-level dry air, cooling induced by the melting and evaporation, etc. [28,29], into CI diagnostics is comparably important. Grabowski and Morrison [30] showed that positive supersaturation noticeably reduced buoyancy and CAPE in the lower troposphere. Peters et al. [31] explained the occurrence of thermal chains by considering the influence of organized entrainment below the updraft's vertical velocity maximum to the cumulus updraft structure. Peters et al. [32] derived a new general lapse rate formula to consider entrainment in CAPE and found that warm biases are evident in previous formulas due to the hydrostatic balance assumption, which neglects the energy sink from buoyancy. All these studies illustrated that the CI is not just passing over the Level of Free Convection (LFC) level for lifted air but occurs when the positive effects are strong enough to overcome the negative effects and thus sustain the upward rushing of unstable air. Recently, Powell [33] studied the criticality of the transition of shallow-to-deep convection and indicated that vertical acceleration inside cloudy updrafts between the cloud base and the zero level was a key quantity controlling the deep convection formation. It is obvious that vertical acceleration is the only quantity that can accurately represent the net effect of the positive and negative processes, thus clearly stating when the positive effects are larger than the negative effects to increase the positive vertical velocity. It is a basic driving force to bring the moist parcel to a "deep" height. At present, there have been extensive studies on the mechanisms and dynamics of deep moist convection (DMC) formation, including the main weather systems, such as cold pools, convergence lines, sea breeze, fronts, and small-scale horizontal convective rolls, and the main controlling dynamic factors, such as the scale of the cloud base, vertical wind shear, humidity, turbulence, and so on [34–36]. However, few studies are concerned with the characteristics of vertical accelerations during the process

of DMC initiations. Powell [33] gave a statistical analysis, but this was for tropical marine convection, which tends to be very different from the convection in dry areas.

In this paper, to study the mechanism of CI during extreme precipitation in southern Xinjiang, the extreme precipitation case that happened on 15 June 2021 in southern Xinjiang (denoted as the "6.15" case) is studied. The vertical acceleration, as the net effect of pressure gradient force (PGF) and Archimedean buoyancy (B), according to the vertical velocity equation, is the focus, with the purpose of finding the main associated physical processes influencing CI in the arid areas in Xinjiang.

The paper is arranged as follows. Section 2 gives an overview of the "6.15" extreme rainfall case in southern Xinjiang, and Section 3 presents the process of the simulation on this case. The general features of vertical accelerations during CI and the associated physical processes are analyzed in Section 4. Conclusions and discussions are presented in Section 5.

2. Case Overview

Features of the precipitation during the "6.15" case are shown in Figure 1. The rainfall data come from the Climate Prediction Center Morphing Technique (Figure 1a, CMORPH, 0.1° × 0.1° grids) and the automatic observation stations' precipitation (Figure 1b) to illustrate the extreme character of the precipitation.

As in Figure 1a, the 24 h precipitation of 15 June 2021 was distributed along the Kunlun Mountains and had an irregular banded structure. Four distributed precipitation centers with 24 h rainfall greater than 50 mm were present, which were much larger than the heavy rainfall standard in Xinjiang (24.1 mm/24 h) [37]. According to the statistics of the local meteorological bureau, the maximum rainfall amount across the whole event reached 121.6 mm, and the daily precipitation reached 74.1 mm in Lop (80.23° E, 37.05° N), which is collocated to the precipitation center (81 mm/24 h, 80.05° E, 37° N) in Figure 1a. The hourly precipitation of five automatic stations in southern Xinjiang is presented in Figure 1b. It shows that strong precipitation mainly appeared during 1200 UTC to 1400 UTC with a maximum value of 20.6 mm in Lop and 28.8 mm in Sampoulu (80.09° E, 36.99° N). The annual average of hourly extreme precipitation was less than 5 mm in this area in the south part of southern Xinjiang. However, from Figure 1b, we see a persistent high precipitation over several hours, which thus caused the extreme precipitation.

Figure 2 shows the radar reflectivities from the local C-band radar in Hotan. It presented a development of the convective cell that is associated with the extreme hourly precipitation in Figure 1b during 1000–1300 UTC. It was found that the cell was produced at approximately (80.75° E, 36.8° N) in the black box in Figure 2a–d embedded in a meso-scale convective system (MCS). The cell reached 30 dBz at 1115 UTC and gradually intensified and moved northwestward through the Sampoulu station (indicated by "1" in Figure 2a) at approximately 1156 UTC with a maximum intensity up to 50 dBz. The extreme precipitation was created by the passing of several such intense convective cells. As is in the red ellipses in Figure 2f–i, they were moving southwestward embedded in another MCS.

Figure 3 presents the synoptic conditions at 0600 UTC 15 June to illustrate several typical weather systems in southern Xinjiang responsible for the extreme precipitation. The most important system is the South Asia High (Figure 3a), the location of which has large influences on Xinjiang precipitation [38,39]. It was near 30° N in this case, and it was coupled with two upper-level westerly jet (ULJ) in its north and a low trough between the two jets. The precipitation region (black box in Figure 3a) was located on the entrance region of the east ULJ with approximately 8×10^{-5} s^{-1} divergence. The trough-jet pattern sustained deeply to the 500 hPa level where the trough region become a low-pressure zone over Xinjiang and its surrounding areas characterized by three short-wave troughs (black dotted lines in Figure 3b). Each trough has contributed to the focused precipitation. The east–west-oriented trough along 40° N transports the cold, dry air from high latitude to southern Xinjiang (yellow arrow), and the north–south-oriented-trough along 72° E approximately has a relatively warm, moist flow from the low latitude toward

the precipitation region (pink arrow), while the other east–west-oriented trough over the mountain near 35° N directed the flow moist easterly (green arrow in Figure 3b) into southern Xinjiang along the north edge of Kunlun Mountain. In the lower levels, southern Xinjiang was characterized by a strong easterly moist wind which entered Xinjiang from its north and went through the Taklimakan Desert to the west of southern Xinjiang. As one of the most important systems for heavy precipitation in southern Xinjiang, the easterly was called the "Tarim easterly jet" locally, which contributes to the transport of moist warm air into the dry area. The jet mostly appears over the boundary layer of 850–700 hPa, which has evident seasonal and daily variations [40,41]. Usually, it is veered in the west of southern Xinjiang under the impact of the surrounding topographies and the pressure structure in the basin. In the current case, the jet moved cyclonically and thus formed a strong convergence with the Kunlun Mountain, which was a main reason for the occurrence of the extreme precipitation.

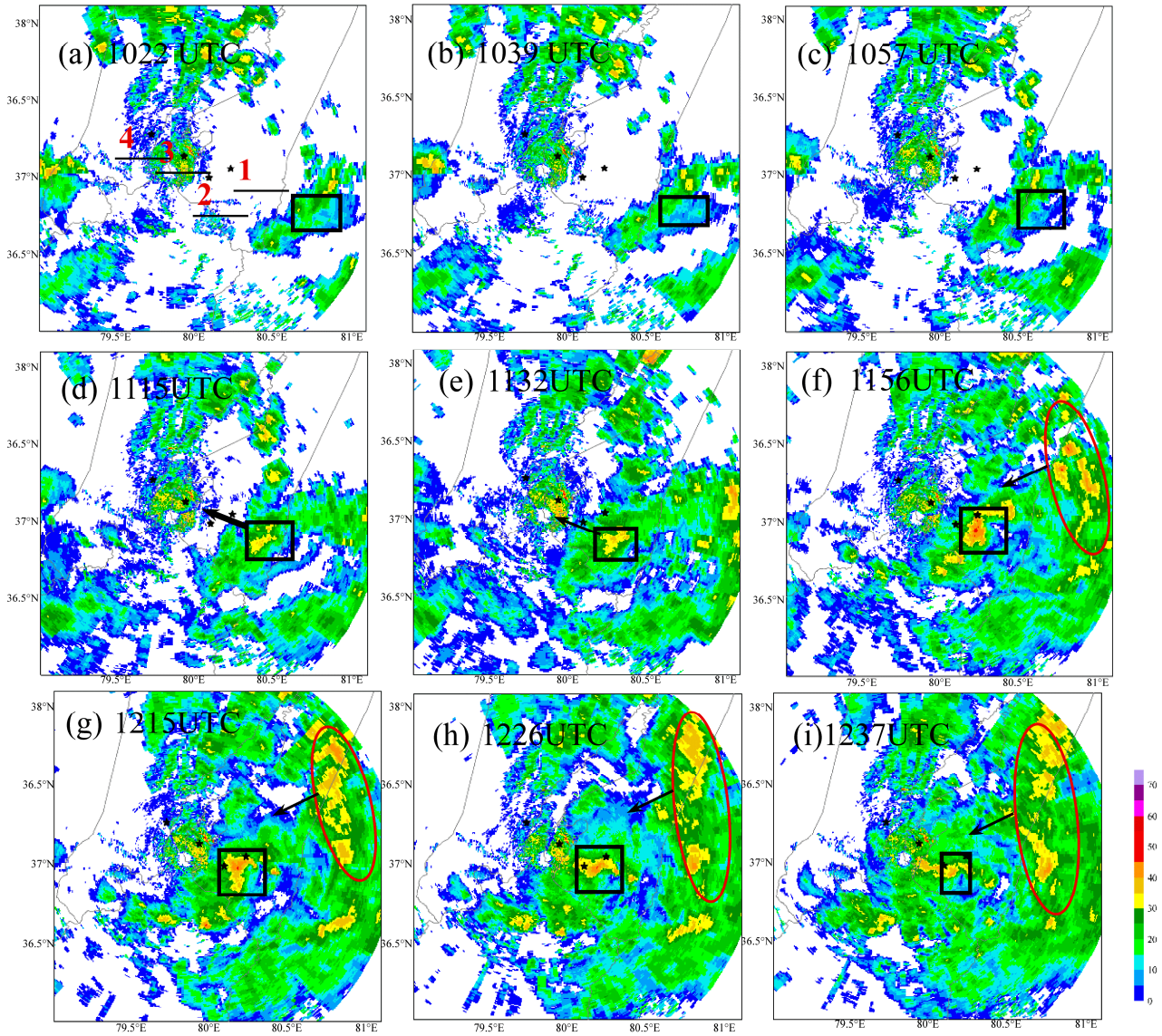

Figure 2. (**a**–**i**) Observed composite radar reflectivity from the C-band radar in Hoton in southern Xinjiang. The stations indicated by the black stars are, respectively, Sampoulu ("1"), Lop ("2"), Hoton ("3"), and Moyu ("4"). The black box and the red circle indicate the focused convective areas.

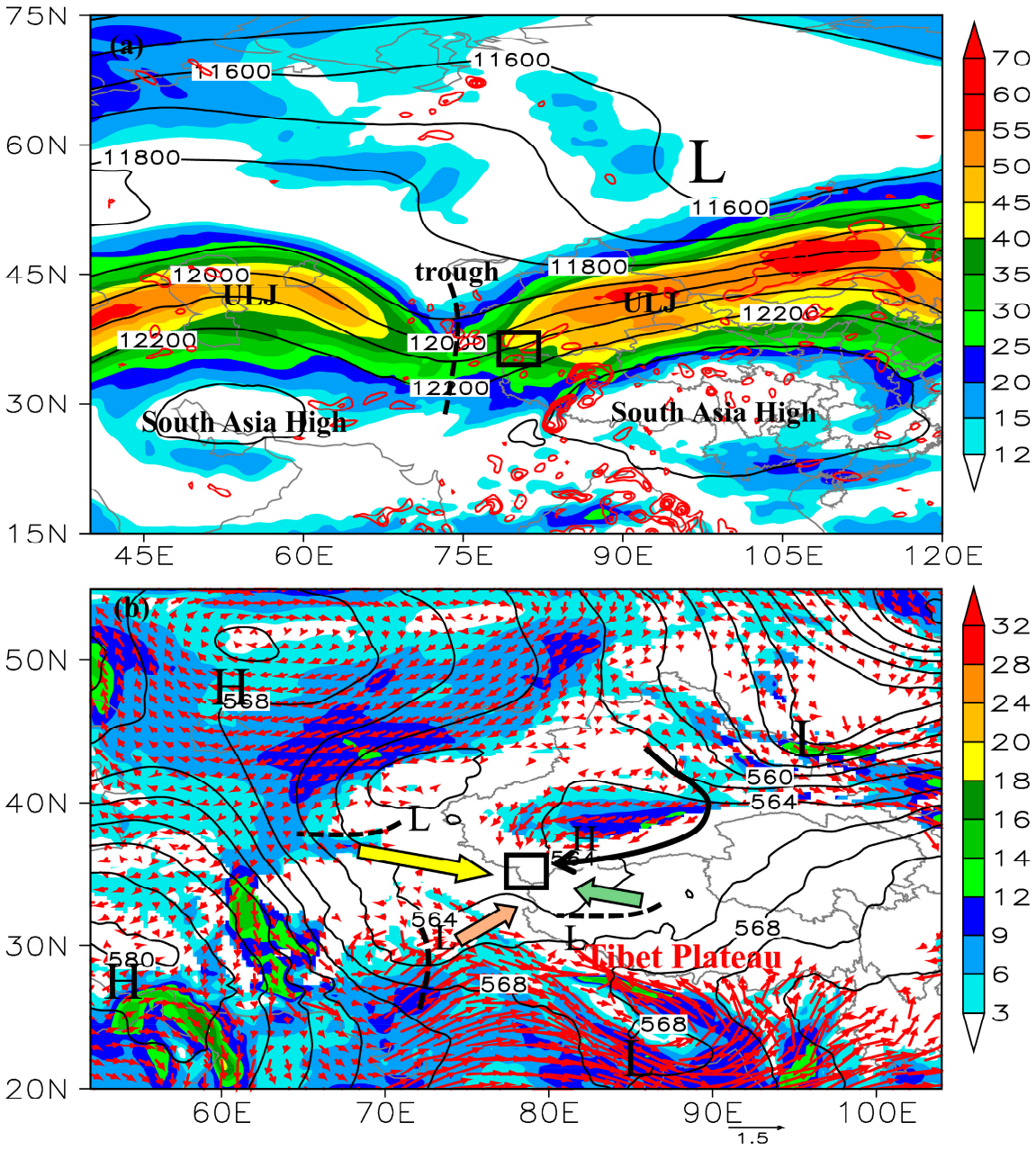

Figure 3. The weather pattern at 1100 UTC on 15 June 2021. (**a**) Geopotential height (black contours, unit: 1 gpm), wind speed (color shaded, unit: m s^{-1}) and horizontal divergence regions (red contours, unit: 10^{-5} s^{-1}, 4 interval) at 200 hPa; (**b**) geopotential height (black contours, unit: 10 gpm) at 500 hPa, and wind speed (color shaded) and water vapor flux (red arrows, unit:) at 800 hPa. The symbol "H" means the high-pressure system and "L" means the low-pressure system, which is denoted by geopotential height in the figures. The black dotted short lines are trough regions. The black boxes indicate the focused precipitation region. The yellow arrow box indicates the flow from the east–west-oriented shallow trough, the pink arrow box indicates the flow from the north–south-oriented shallow trough and the green arrow indicates the flow from the east–west-oriented shallow trough over the mountain. The black thick arrows indicate the main directions of the moisture transportation.

3. Methods

A high-resolution simulation of the "6.15" case is conducted considering the limited observations in southern Xinjiang. The configuration of the model can be found in the Supplement Files. Although the simulated extreme precipitation is more west than the

observations (also see Supplement Files), an examination of the successive hourly precipitation and radar reflectivities indicates that the long-lasting characteristic of strong precipitation over a limited area to produce the rare disastrous precipitation is well expressed in the model, which is similar to the observations (Figure 2). Figure 4 presents a development of a strong convective cell in the simulation that highly resembles the cell development in Figure 2. It was produced at approximately 0800 UTC with maximum radar reflectivity larger than 35 dBz (the box in Figure 4d). Then, it experienced the growth and reached the largest intensity at approximately 1200 UTC. The convective cell had a sedentary life and contributed to the largest precipitation in the extreme precipitation center in WRF simulation. As in Figure 4, the hourly rainfall accompanying the cell showed a maximum intensity of 24 mm/h.

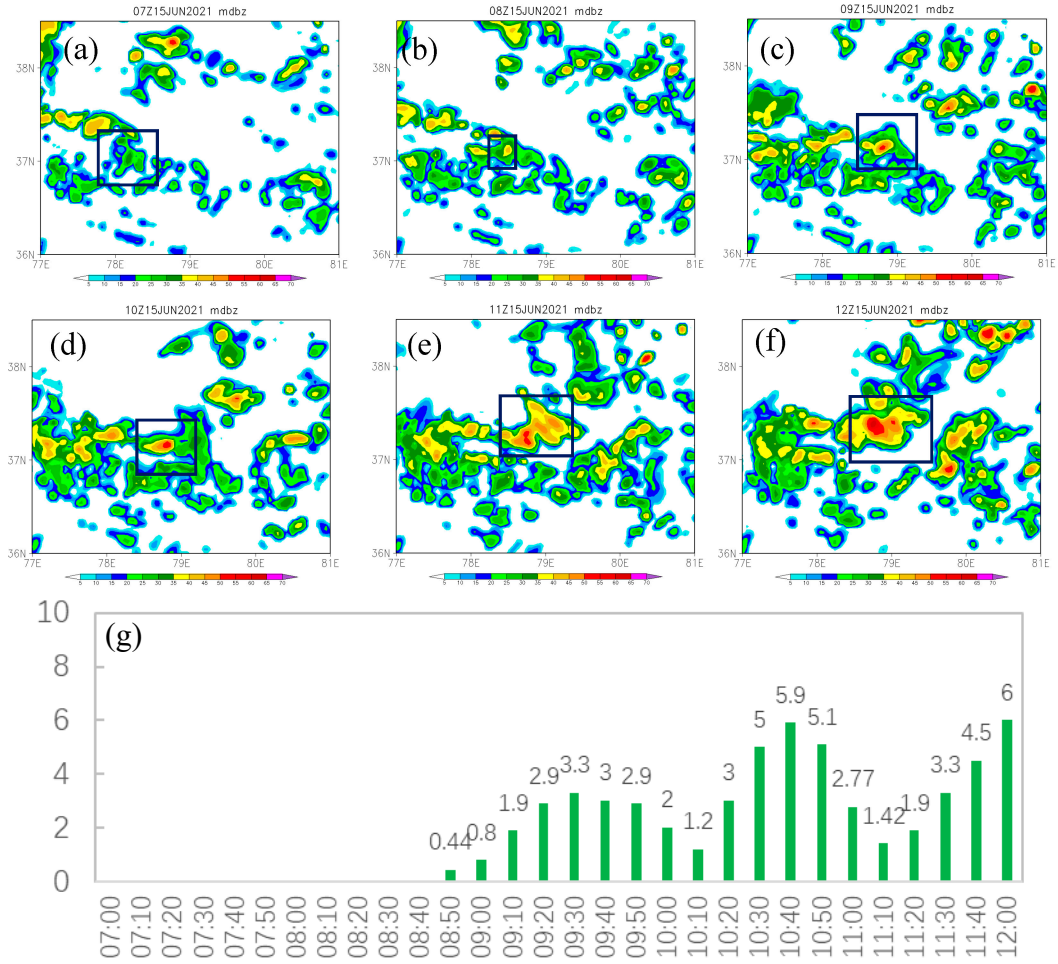

Figure 4. Simulated maximum radar reflectivities at (**a**) 0700 UTC, (**b**) 0800 UTC, (**c**) 0900 UTC, (**d**) 1000 UTC, (**e**) 1100 UTC, (**f**) 1200 UTC on 15 June 2021. Boxes enclosed the convective cell that the paper concerned. (**g**) The bar chart is the 10-min precipitation during this period.

The convections in Xinjiang have a common feature in that they are often dispersedly distributed and looking unorganized due to the influence of complex terrain, the complex gravity waves induced by the terrain and the special oasis-desert-coexisted land surfaces, which can be seen in both the observation and simulations [27]. Thus, the associated precipitation is often not large. However, in the "6.15" case appeared the slow-moving and intense extreme-precipitation-producing convective cell. So, how did this strong convection develop in such dry areas where the annual precipitation is only 30–50 mm? In the following research, we will focus on the inner dynamics of the initiation process of the strong convection and thus find the key mechanism controlling the occurrence of the extreme precipitation in southern Xinjiang.

4. Results

4.1. Vertical Acceleration as a Basic Force for CI

Deep convection is essentially the development of vertical updraft, and vertical acceleration is a basic force to the vertical updraft and also an essential process that the convection must experience to reach a sufficient height. The dynamics controlling CI are thus naturally described by the vertical velocity equation [42]:

$$\frac{dw}{dt} = -\frac{1}{\rho}\frac{\partial p}{\partial z} - g \tag{1}$$

where dw/dt is the vertical acceleration of an air parcel with unit mass, $-1/\rho(\partial p/\partial z)$ is the acceleration due to vertical pressure gradient force, and g is gravitational acceleration. Equation (1) attributes the vertical acceleration of air particles to the net effect of the vertical pressure gradient force and gravity. Here, we use Net_WAz1 to denote this net effect.

By extracting a horizontally homogeneous, static-balanced base state from the total pressure p and density field ρ ($p' = p - \overline{p}(z)$, $\rho' = \rho - \overline{\rho}(z)$), the vertical velocity equation becomes

$$\frac{dw}{dt} = -\frac{1}{\overline{\rho}}\frac{\partial p'}{\partial z} - \frac{\rho'}{\overline{\rho}}g, \tag{2}$$

in which the acceleration is determined by the net effect of a vertical perturbation pressure gradient force (PGF) $-1/\overline{\rho}(\partial p'/\partial z)$ and the buoyancy $B = -g\rho'/\overline{\rho}$ (denoted as Net_WAz2) [17].

The above framework has been extensively used to diagnose the dynamics of convective phenomena, including squall lines, downbursts, rear inflow jet as well as CI [43,44]. They present many important physical processes that implicitly act on the convection.

In principle, no matter how to treat the right-hand side of the above vertical velocity equations, the vertical acceleration dw/dt should be unchanged. To calculate the above equations with WRF data, a usual treatment is first remapping the model's fields in the WRF η coordinate into the height coordinate and then calculating the terms associated with PGF and B with a proper base state [44]. However, interpolation errors are likely to appear during the remapping and the vertical differential calculations, especially around complex high terrains. These errors may be reasonably small when the terrain is flat or the accelerations dw/dt are large such as in the rapid-development stage of the storm. However, in southern Xinjiang where it is difficult for the convection to become large and deep, plus the presence of very complex and steep topography, it is difficult to obtain balanced results of the Net_WAz1 or Net_WAz2 to the dw/dt in Equations (1) and (2).

To avoid the interpolation error problem, an alternative method is to analyze the vertical velocity equation directly from the model in the WRF η coordinate which controls the details of the cloud development [42]:

$$\begin{aligned} &\partial W/\partial t + m_x\left[\partial_x(Uw) + \partial_y(Vw)\right] + \partial_\eta(\Omega w) \\ &= m_y^{-1} g(\alpha/\alpha_d)\left[\partial_\eta p' - \overline{\mu}_d(q_v + q_c + q_r)\right] - m_y^{-1}\mu_d' g \end{aligned}, \tag{3}$$

where $U = \mu_d u/m_y$, $V = \mu_d v/m_y$, $W = \mu_d w/m_y$ are the redefined prognostic variables, $\mu_d = \partial p_d/\partial\eta$, m_x and m_y are the map-scale factors, p' and μ_d' are perturbations to the domain-averaged pressure $\overline{p}(z)$ and $\overline{\mu}_d$; q_v, q_c and q_r are, respectively, the mixing ratios of water vapor, cloud water and rain water; α_d is the inverse density of the dry air ($1/\rho_d$) and α is the inverse density taking into account the full parcel density $\alpha = \alpha_d(1 + q_v + q_c + q_r + q_i + q_s)^{-1}$; the vertical diffusion has been ignored due to its small value.

Since the mass-based quantity μ_d satisfies [45]:

$$\partial\mu_d/\partial t + m_x m_y\left(U_x + V_y\right) + m_y\partial_\eta\Omega = 0, \tag{4}$$

it can be derived that the terms on the right-hand side of Equation (3) denote the net accelerations (denoted as Net_WAη) in the η coordinate by a magnitude of μ_d, that is $dw/dt = (Net\_WA\eta)/\mu_d = Net\_WAz1 = Net\_WAz2$. The PGF values in Equations (2) and (3) can also find their own corresponding form. Moreover,

$$g(\alpha/\alpha_d)\partial_\eta p' = g(\alpha/\alpha_d)\partial_\eta z \partial_z p' = \mu_d(\alpha\partial_z p') \approx \mu_d \frac{1}{\overline{\rho}}\partial_z p'. \quad (5)$$

Then, the residual part of the terms

$$m_y^{-1} g(\alpha/\alpha_d)[-\overline{\mu}_d(q_v + q_c + q_r)] - m_y^{-1}\mu_d' g \quad (6)$$

on the right-hand side of Equation (3) can be attributed to the buoyancy $-\frac{\rho'}{\overline{\rho}}g$, including the drag of hydrometer mixing ratios. By a minor change in the WRF model output procedure, we are able to output Net_WAη, and PGF and B in Equations (5) and (6).

A difference of Net_WAz1 and Net_WAz2 calculated from Equations (1) and (2) to Net_WAη which is directly output from the WRF model is shown in the Supplementary Files. It verifies that using the WRF output Net_WAη best matches the accelerations within the model. In the following analysis, we will use the Net_WAη to analyze the vertical accelerations during CI for extreme events.

4.2. Global Features of Vertical Accelerations During CI

According to the height of the cloud top which is denoted by the total mixing ratio of cloud and ice particles, the development of the focused convective cell (Figure 4) is divided into two stages: the nascent stage and the deep-convection stage.

In the nascent stage, as shown in Figure 5, a cumulus grows over the north side of Kunlun Mountain between 37 and 37.2° N (Figure 5c,d). This stage continued about 2.5 h from 0600 UTC to 0830 UTC during which the development is dilatory. Although the composite radar reflectivity reached the 35 dBz standard for CI, it is actually not "triggered" to form the deep convection, as the cloud top is only 2 km to the surface. The vertical velocity is confined to 0.5–2 m/s with the largest value mainly located near the cloud base (Figure 5c,d).

After this stage, from 0900 UTC, the cloud top rushed up to 8 km height in 30 min, after which it is considered that the deep convection is initiated (Figure 6). This formed a sharp comparison to the slow-developing nascent stage. The vertical velocity is 3–4 m/s (Figure 6d–f), and the ascending center is much higher than the nascent stage, locating on the upper part of the cumulus. Meanwhile, the descending in the lower levels appears beneath the ascending areas.

Vertical accelerations denoted by Net_WAη corresponding to the above process are given in Figures 5 and 6. In the nascent stage, we see two types of Net_WAη in the sub-cloud layer and within the cloud with two representative times, respectively, at 0750 UTC and 0820 UTC (Figure 5e,f). At 0750 UTC (Figure 5e), Net_WAη performs a strong positive value in the sub-cloud layer, which indicates strong acceleration of the ascending air into the cloud. However, at 0820 UTC (Figure 5f), Net_WAη exhibits unanimous negative values both in and below the cloud. Most of the negative Net_WAη corresponds to a downward motion (Figure 5d) beneath the cloud center, but some extends the ascending areas, thus inhibiting the upward development of the cloud.

In the deep convection stage (Figure 6g–i), Net_WAη all becomes positive over the height of the cloud with two large positive centers. One center is below the cloud top, which is responsible for accelerating the upper-level cloud air to form the deep convection, while the other is in the lower levels between the cloud base and 0 °C level (black dotted line), which can accelerate and sustain the low-level upward motions to draw in the moist air from the boundary layers.

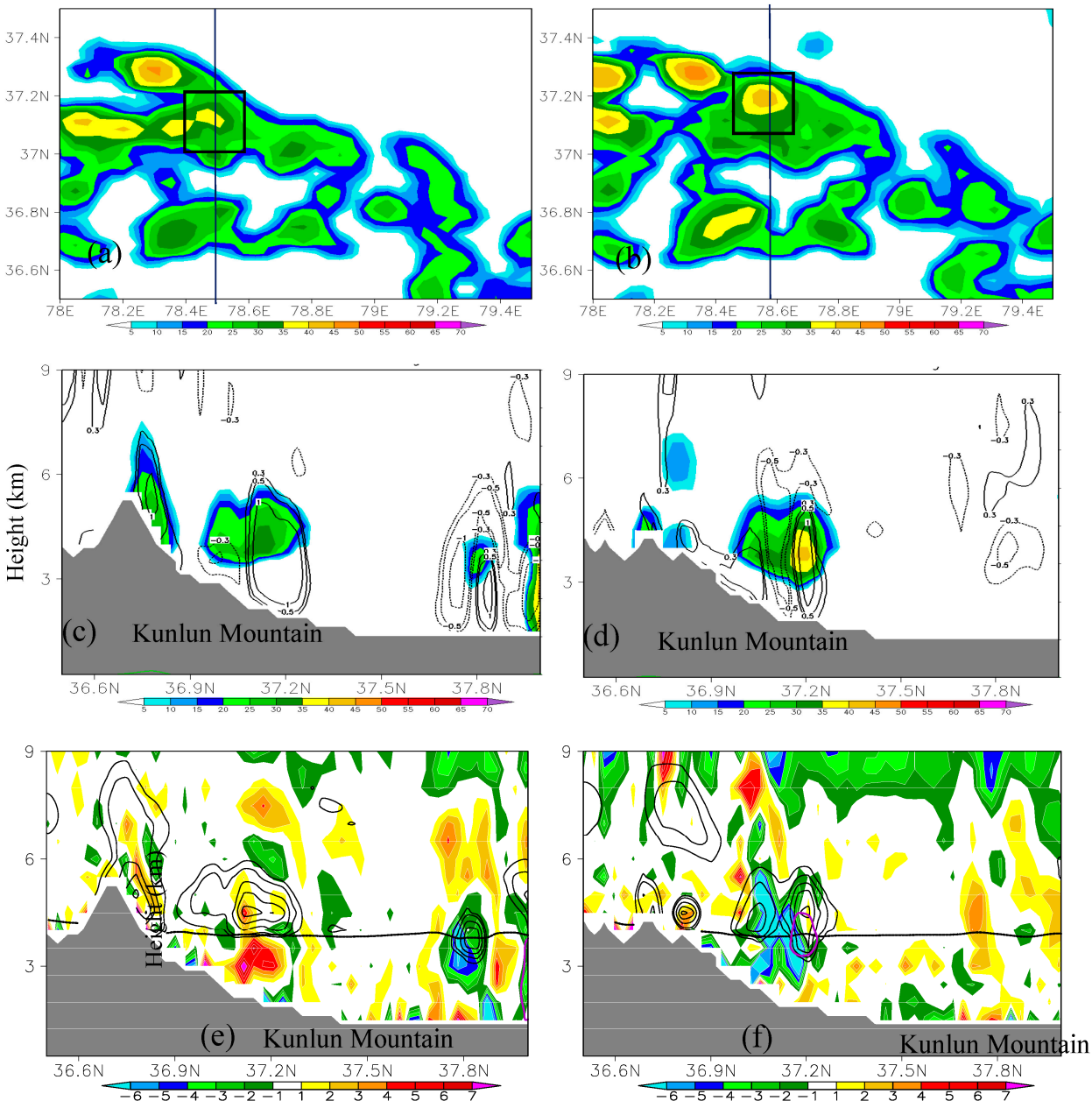

Figure 5. (**a**,**b**) Maximum radar reflectivity (shaded, unit: dBz); (**c**,**d**) radar reflectivity (shaded, unit: dBz) and vertical velocity (contour, unit: m s^{-1}); and (**e**,**f**) vertical accelerations denoted by Net_WAη (shaded, unit: 10^{-3} s^{-1}) and sum of mixing ratios of ice and cloud particles (0.05, 0.1, 0.2, 0.3, 0.4 black contours, unit: g/kg) at 0750 UTC along 78.5° E (left column) and 0820 UTC along 78.6° E (right column). The purple contour in (**f**) is 35 dBz radar reflectivity. The thick black line is 0 °C isotherm contour.

From the above analysis, during the whole development process of the focused convection, a significant signature of CI is the formation of the persistent positive Net_WAη within the cloud, meaning the appearance of the positive force for the vertical motions in the cloud. Before the persistent positive Net_WAη, the development of the cumulus is tardy, as indicated above, which is a shallow or nascent convection stage. With the in-cloud positive Net_WAη appearing, the convection rapidly becomes deep. This implies that vertical acceleration may be a dominant feature for the transition of the shallow to the deep convection. Powell [33] noticed the relation of the vertical acceleration (they called it "effective buoyancy" by ignoring the effect of dynamic pressure) and the criticality of the

shallow-to-deep transition of simulated marine convection. He found that there is a critical value of vertical accelerations between the cloud base and 0 °C level to control the deep convection initiation and, moreover, a robust relationship exists between vertical acceleration and rain rate. The results of Powell [33] are clearly demonstrated in Figures 5 and 6. But the difference is the strong acceleration in the levels between the cloud top and 0 °C level, which is considered to be responsible for the height that the convection can develop. The transition of shallow to deep convection of the focused cumulus occurs at approximately 0900–09100 UTC (Figure 6g) when Net_WAη between the cloud base and the 0 °C level reaches about 5×10^{-3} s^{-1} and that between the cloud top and the 0 °C level also reaches up to 5×10^{-3} s^{-1}. This amount is equal to a 0.3 m/s acceleration of vertical velocity in 10 min.

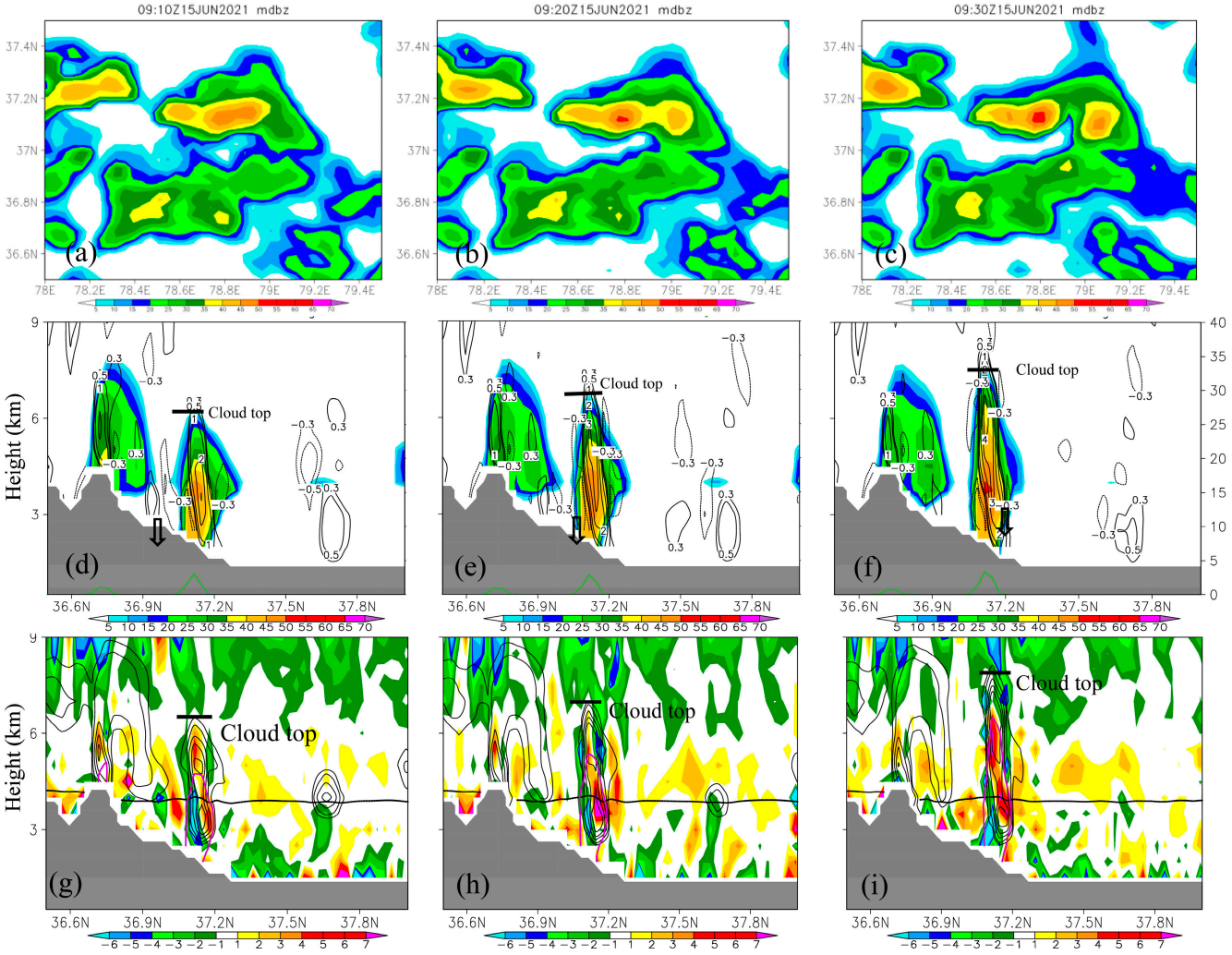

Figure 6. (**a**–**c**) Maximum radar reflectivity (shaded, unit: dBz); (**d**–**f**) radar reflectivity (shaded, unit: dBz) and vertical velocity (contour, unit: m s^{-1}); and (**g**–**i**) vertical accelerations denoted by Net_WAη (shaded, unit: 10^{-3} s^{-1}) and the sum of mixing ratios of ice and cloud particles (0.05, 0.1, 0.2, 0.3, 0.4 values, unit: g/kg) at 0910 UTC (left column), 0920 (middle column) and 0930 UTC (right column) along 78.8° E. The purple contour in (**g**–**i**) is 35 dBz radar reflectivity. The thick black line is the 0 °C isotherm contour. The green lines in (**d**–**f**) indicate 1 h precipitation (unit: mm) with magnitude on the right side of the y-axis.

4.3. Possible Processes Influencing the Convection Initiation

From the point view of forecast, a critical value that is able to distinguish the shallow to deep transitions is of great use. However, the transition is more like a process, not just

a point, which is closely related to when the in-cloud positive Net_WAη becomes strong enough to break through the inhibition of strong negative Net_WAη. In Figures 5 and 6, the process of CI has three evident vertical acceleration stages: the sub-cloud acceleration; then the negative Net_WAη denoting deceleration in cloud; finally the cloud-top accelerations. It is worth finding the implied physical processes associated with these accelerations, thus giving a deeper understanding of CI in the extreme rainfall process in southern Xinjiang.

4.3.1. The Sub-Cloud Vertical Acceleration

The sub-cloud lifting is necessary by bringing the air parcel to the height of LFC. In the nascent stage, as in Figure 5e, the strong positive Net_WAη in the sub-cloud layer under the height of LFC performs as a lifting force for accelerating the ascending parcel into the cloud. However, about 40 min ago at 0710 UTC, when the most initial cloud appears, there is no such strong acceleration.

The components of Net_WAη including the PGF (Equation (5), denoted as PGF_WRF) and B (Equation (6), denoted as B_WRF) are shown in Figure 7, respectively, at 0710 UTC and 0750 UTC, including the difference of these two times. Here, the PGF and B are denoted as PGF_WRF and B_WRF because they are directly output from WRF simulation. The perturbations in them are relative to the initial fields of the model rather than the real environment generally represented by the so-called base state. Due to this reason, B_WRF here is also not a true buoyancy that exerts to an air parcel. Therefore, as in Figure 7b,e, B_WRF performs strong negative values over the Kunlun Mountain either within or out of the cloud. On the contrary, the PGF_WRF is mostly positive values (Figure 7a,d), which are cancelled with B_WRF. In Figure 7c,f, three regions are enclosed by the boxes with different colors, respectively denoting the in-cloud area (orange box), the sub-cloud area (blue box) and the boundary-layer area in front of the convection (green box). At 0710 UTC, PGF_WRF and B_WRF are almost all offset in the piedmont boundary-layer area (green box) and the in-cloud area (yellow box), indicating nearly hydrostatic balance in these two areas, while the magnitude of PGF_WRF is a little larger than B_WRF in the sub-cloud layer (blue box), indicating a weakly non-hydrostatic state. Then, at 0750 UTC, the piedmont boundary layer (green box in Figure 7f) is still hydrostatic with PGF_WRF and B_WRF all offset, while the sub-cloud layer and in-cloud layer become strongly non-hydrostatic with large accelerations. Therefore, it may be concluded that PGF_WRF performs a larger effect on the sub-cloud strong acceleration in Figure 7c, f because it is positive.

However, the change in the PGF_WRF and B_WRF from 0710 UTC to 0750 UTC in Figure 7g,h reveals that B_WRF also makes contributions. As in Figure 7g, the PGF_WRF difference presents strong positive values in both the piedmont boundary layer (green box in Figure 7g), the sub-cloud layer (blue box in Figure 7g) and the in-cloud layer (orange box in Figure 7g), while the B_WRF difference (Figure 7h) mainly shows a negative value in the corresponding areas. But the B_WRF difference is strongly negative in the cloud (orange box in Figure 7h) and in the piedmont boundary layer (green box in Figure 7h), largely offsetting the positive PGF_WRF difference. The B_WRF in the sub-cloud layer is nearly zero (blue box in Figure 7h), making a larger difference of Net_WAη in the sub-cloud layer (blue box in Figure 7i). Thus, we believe that the large positive change in PGF_WRF and the small near-zero change in negative B_WRF in the sub-cloud layer from 0710 UTC to 0750 UTC (Figure 7g) both contribute to the sub-cloud acceleration.

To find the inner physical processes associated with PGF_WRF, the linear diagnostic relation for perturbation pressure reference to the initial base state is involved,

$$p' = \frac{c_p}{c_v}\overline{p}\left(\frac{\theta'}{\overline{\theta}} - \frac{\alpha'_d}{\alpha_d} + 1.61{*}q_v\right) \tag{7}$$

where c_p and c_v represent the specific heat at constant pressure and constant volume, respectively, θ is the potential temperature and θ' is its perturbation. The equation is derived from the state equation and is consistent with the pressure diagnostic relation of the WRF model [45]. It shows that the perturbation pressure (reference to the initial state)

is composed of three parts: the thermodynamic pressure ($p'_\theta = \frac{c_p}{c_v}\overline{p}\frac{\theta'}{\overline{\theta}}$), the density-related pressure ($p'_\rho = -\frac{c_p}{c_v}\overline{p}\frac{\alpha'_d}{\alpha_d}$) and the moisture-related pressure ($p'_m = 1.61\frac{c_p}{c_v}\overline{p}q_v$). Any factors in the WRF model can influence the perturbation pressure as long as they affect the perturbation potential temperature, perturbation density and moisture, such as diabatic heating and cooling (according to the thermodynamic equation), divergence and convergence (according to the continuity equation), and also moistening of the air. The perturbation pressure calculated from Equation (7) is verified to be almost identical to the WRF-output perturbation pressure. Therefore, we are able to decompose the perturbation pressure into three parts. Figure 8 directly presents the pressure difference between 0710 UTC and 0750 UTC (pressures at 0750 UTC minus those at 0710 UTC) of each part.

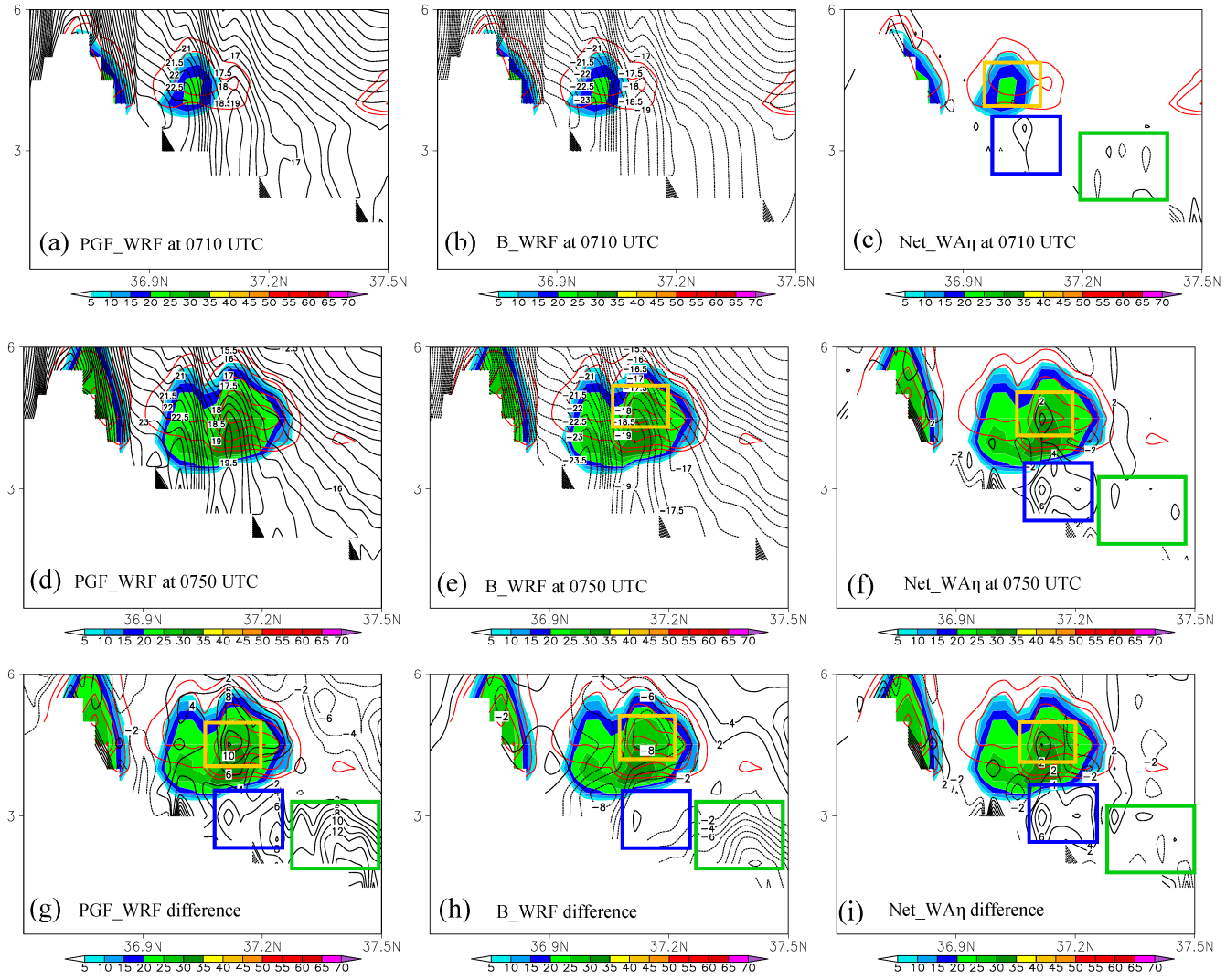

Figure 7. (**a**) PGF_WRF, (**b**) B_WRF and (**c**) Net_WAη at 0710 UTC along 78.5° N (contours, unit: 10^{-3} s^{-1}); (**d**–**f**) same as (**a**–**c**) but for 0750 UTC; (**g**) PGF_WRF difference, (**h**) B_WRF difference, and (**i**) Net_WAη difference between 0750 UTC and 0710 UTC along 78.5° N. The shaded areas are radar reflectivities. The red contours are the sum of mixing ratios of ice and cloud particles (0.05, 0.1, 0.2, 0.3, 0.4 values, unit: g/kg) to indicate the cloud. The "difference" means the fields at 0750 UTC minus those at 0710 UTC. The colored boxes indicate the areas with evident differences between 0710 and 0750 UTC. The areas enclosed by the orange box, blue box and green box are, respectively, the in-cloud area, the sub-cloud area and the boundary-layer area in front of the convection.

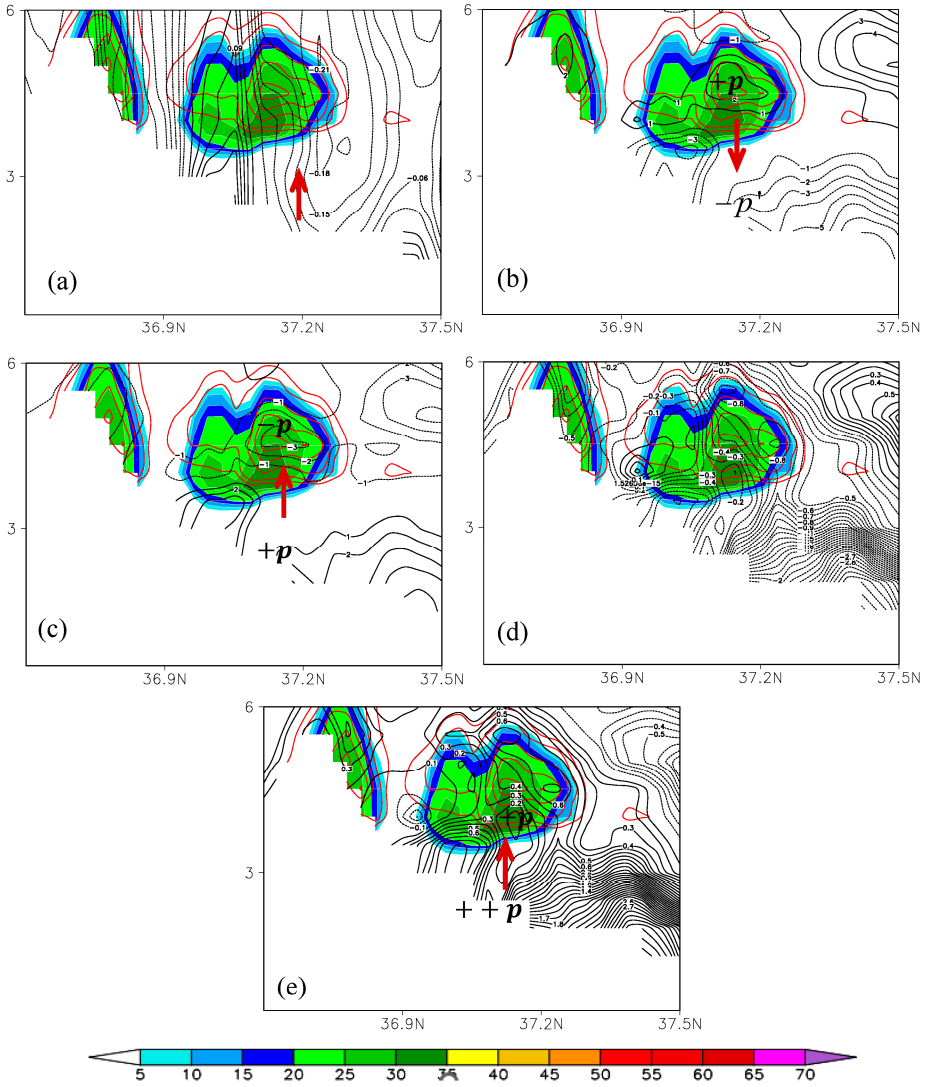

Figure 8. (**a**) Difference of perturbation pressure between 0710 UTC and 0750 UTC (contours, unit: hPa) along 78.5° N; (**b**) same as (**a**) but for p'_θ; (**c**) same as (**a**) but for p'_ρ; (**d**) same as (**a**) but for $p'_\rho + p'_\theta$; (**e**) same as (**a**) but for p'_m. The shaded areas are radar reflectivities. The red contours are the sum of mixing ratios of ice and cloud particles (0.05, 0.1, 0.2, 0.3, 0.4 values, unit: g/kg) to indicate the cloud area. The "difference" means the fields at 0750 UTC minus those at 0710 UTC. The red thick arrows indicate the direction of PGF due to the change in the corresponding perturbation pressure.

In Figure 8a, it can be found that the convective areas that we are concerned with presented a decrease in perturbation pressure between 0710 UTC and 0750 UTC. Since the pressure decrease in the boundary is not as large as that in the cloud, an upward PGF change is induced (red arrow in Figure 8a), which is consistent with the PGF_WRF change in Figure 7g.

p'_θ shows a positive change in the cloud and a negative value in the boundary layer, as indicated by the difference between 0710 and 0750 UTC in Figure 8b. It is related to an in-cloud heating and a sub-cloud cooling during the cloud development, thus forming the downward PGF change from 0710 UTC to 0750 UTC (red arrow in Figure 8b). For p'_ρ, the circumstance is inverse with a decrease in density (increase in specific volume) in cloud and increase in density in the sub-cloud layer (decrease in specific volume), resulting in an upward PGF difference (Figure 8c). However, the sum of these two terms induced a downward PGF change in Figure 8d, representing a whole change in the PGF of the dry air and opposite to the total change in PGF, as shown in Figure 8a. p'_m presents an evident

increase in the boundary layer (Figure 8e) from 0710 UTC to 0750 UTC, which thus induced an upward PGF change. This upward PGF increment is a main source of the positive PGF_WRF and Net_WAη in the sub-cloud layer at 0750 UTC in the nascent stage, which indicates a significant and direct role of moisture concentration in the vertical accelerations.

The change in p'_m is due to the moistening of the boundary layer (Figure 9a,b). The moisture distribution and its flux around the focused cumulus are shown in Figure 9. From 0710 UTC to 0750 UTC, the moisture presents an evident increase by about 0.6 g/kg with its vertical gradient enhanced (black boxes in Figure 9). The magnitude of the horizontal water vapor flux shows a maximum near the surface layer at about 37.4° N, indicating a strong moisture transportation by a boundary-layer jet which climbs up the mountain (Figure 9e,f).

As indicated above, apart from the positive PGF_WRF change, the other factor contributing to the sub-cloud acceleration is the near-zero change in B_WRF, which actually highlights the positive PGF_WRF by diminishing negative effects by B_WRF. According to Equation (6), this is likely to be related to μ'_d, which is further attributed to the divergence as in Equation (4). Figure 9g–j presented both the two-dimensional (2D) and three-dimensional (3D) wind divergence along the developing cumulous. For 2D divergence, one can find the typical picture of low-level convergence superposed by mid-level divergence, corresponding to an ascent. However, for the 3D divergence, the pattern is nearly reversed with a low-level 3D divergence superposed by mid-level 3D convergence, indicating a high compressibility property of the convective atmosphere. Moreover, a high correlation of the 3D divergence pattern to the B_WRF difference in Figure 7h can be found with 3D convergent areas mostly having large negative B_WRF differences, such as the in-cloud layer and the boundary layer. In the sub-cloud layer where there is 3D divergence, the B_WRF difference is weak positively. This is consistent with Equations (4)–(6), because a 3D convergence tends to cause an increase in μ'_d, making a decrease in B_WRF; while a 3D divergence can decrease the mass in the column, which can then increase the B_WRF, such as in the sub-cloud layer. A minus of μ'_d at 0750 and 0710 UTC ($\mu'_d|_{0750UTC} - \mu'_d|_{0710UTC}$, green lines in Figure 9h,j) demonstrates the above result, as it shows a strong negative value in the convective area.

The above analysis indicates a significant role of the moisture and the 3D divergence to the nascent development of the cumulous before CI from the altitude of the vertical accelerations. Different from the previous studies which emphasized the effect of moisture on the buoyancy by heating the atmosphere through condensation, this study found that in the WRF model, moisture can directly influence the vertical acceleration by PGF. Also different from a common understanding of the role of the 2D convergence by concentrating the moisture and affecting the lifting, it is found that 3D divergence is more directly related to vertical acceleration.

4.3.2. The In-Cloud Decelerations to Inhibit the Convection Initiation

With a strong sub-cloud acceleration, it was anticipated that the convection could rapidly develop deep to produce strong precipitation. However, as stated in Section 4, despite the 35 dBz maximum radar reflectivity during the nascent stage, the cloud top did not develop high to form deep convection until 0910 UTC. So, what did the cloud cell encounter during the following hour after a favorable development at 0700–0800 UTC? Figure 8f presents a relatively small positive or even negative Net_WAη within the cloud which inhibits the upward development of the convection. A detailed understanding of this negative Net_WAη is important because it influences the convection initiation time by restraining the convection development.

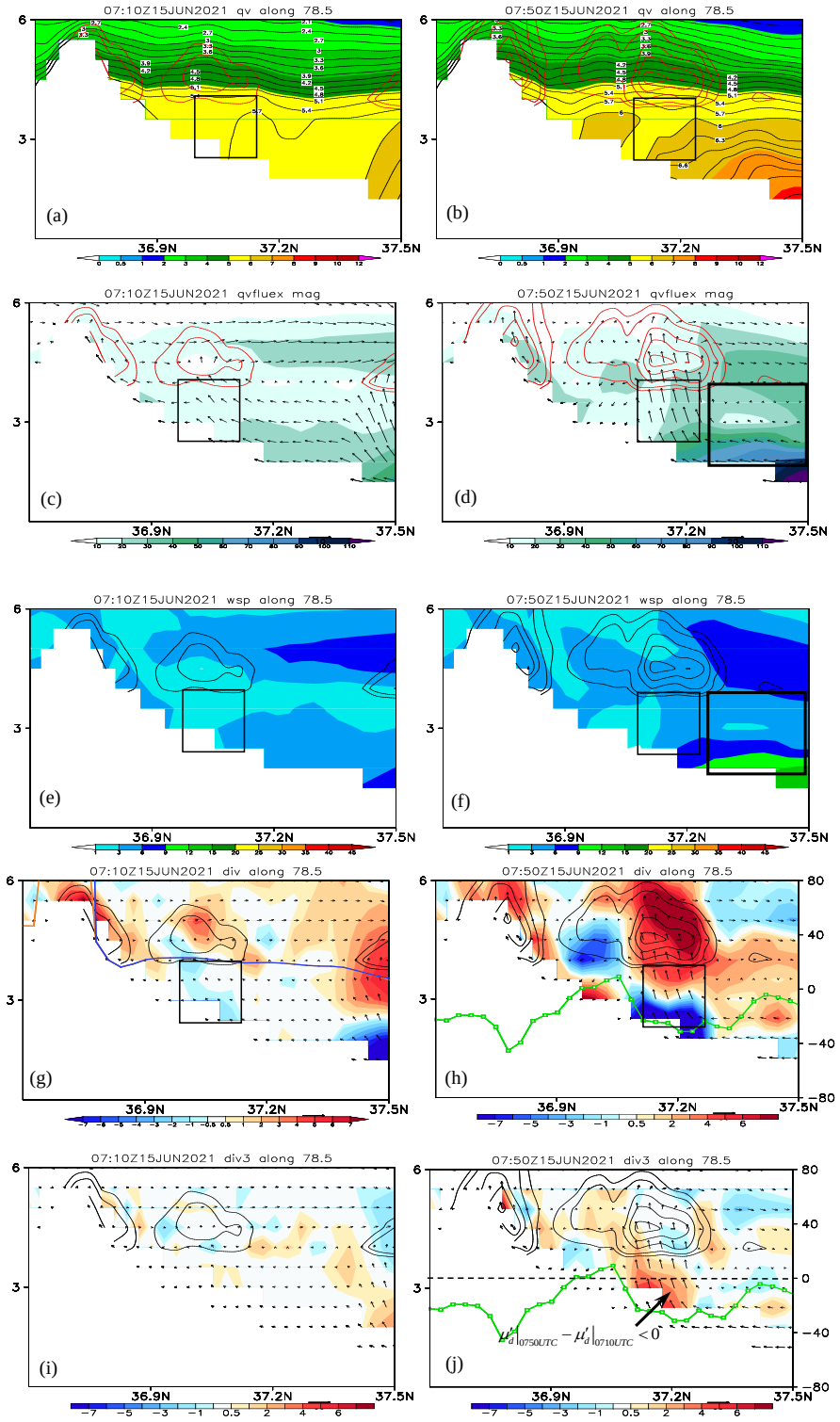

Figure 9. (**a**,**b**) Water vapor mixing ratio (shaded and black contours, unit: g/kg); (**c**,**d**) magnitude of water vapor flux (shaded) and wind vectors of (v, w) (unit: m/s); (**e**,**f**) horizontal wind speed; (**g**,**h**) 2D horizontal divergence (shaded, unit: 10^{-4} s^{-1}) and wind vectors of (v, w) (unit: m/s); and (**i**,**j**) 3D horizontal divergence (shaded, unit: 10^{-4} s^{-1}) and wind vectors of (v, w) (unit: m/s) in the section at 0710 UTC (left column) and 0750 UTC (right column) along 78.5° N. The red contours are the sum of mixing ratios of ice and cloud particles (0.05, 0.1, 0.2, 0.3, 0.4 values, unit: g/kg) to indicate the cloud. The blue line in (**e**,**f**) is the free convection level, and the orange line is the condensation level. The green line in (**j**) is the minus of the mass in column at 0750 and 0710 UTC ($\mu'_d|_{0750UTC} - \mu'_d|_{0710UTC}$).

Figure 10 gives a distribution of PGF_WRF and B_WRF along the cloud core at 0820 UTC through 76.6° E. A comparison of Figure 7d–f to Figure 10 shows that the decrease in PGF_WRF in the cloud, which thus makes it smaller than the magnitude of B_WRF, may be a main reason for the negative Net_WAη at 0820 UTC. Compared to B_WRF near the cloud core at 0750 UTC, the negative B_WRF in Figure 10b at 0820 UTC presents an increase from approximately −19~−17 s^{-1} (orange box in Figure 7e) to −19~−15 s^{-1} (orange box in Figure 10b), which cannot contribute to the negative Net_WAη (Figure 10c).

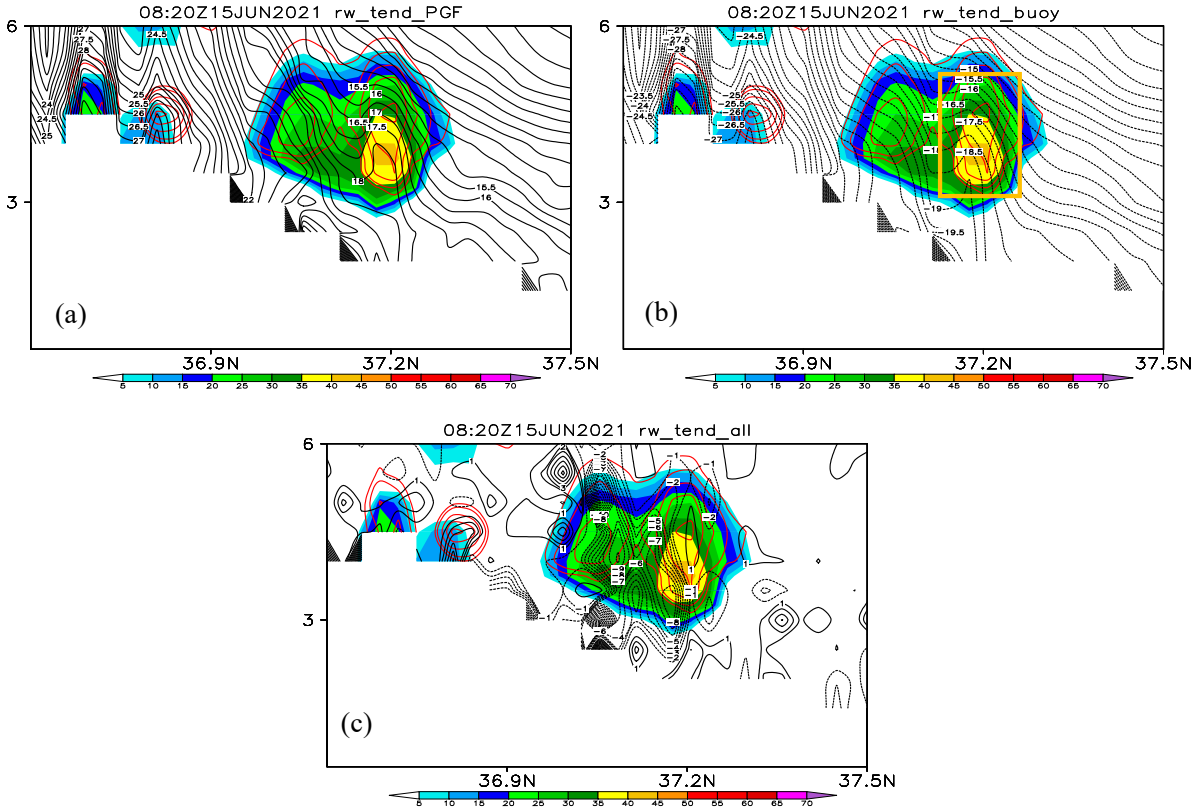

Figure 10. (**a**) PGF_WRF, (**b**) B_WRF and (**c**) their sum for Net_WAη at 0820 UTC (contours, unit: 10^{-3} s^{-1}) along 78.6° N. The shaded areas are radar reflectivities. The red contours are the sum of mixing ratios of ice and cloud particles (0.05, 0.1, 0.2, 0.3, 0.4 values, unit: g/kg) to indicate the cloud.

To find the responsible factor, Figure 11 presents the perturbation pressure and its components at 0820 UTC along the cloud core. A comparison of Figure 11e to Figure 8n at 0750 UTC shows that the sub-cloud p'_m is sustainably increasing due to the greater moisture accumulation in the boundary layer, thus further enhancing the upward PGF. However, the sum of p'_θ and p'_ρ in Figure 11d presents an enhancement of downward PGF compared to Figure 8k as the pressure contours near the cloud core become dense in the vertical direction. Then, a comparison of Figure 11b,c and Figure 8b,e shows that this is mainly related to a decrease in p'_θ within the cloud, which is most evident at 4–5 km levels near 37.1–37.2° N (black box in Figure 11b). From the definition of p'_θ, this is related to an in-cloud decrease in θ' from 0750 UTC to 0820 UTC, which is thus a main factor responsible for the in-cloud negative Net_WAη or in-cloud deceleration at this time.

The temperature perturbation T_l corresponding to θ' is shown in Figure 12. In Figure 12a,b, one can find a relatively cold layer superposing on a warm boundary layer below 6 km. The cloud core is becoming warmer than its surrounding area with the development of the cloud from 0750 UTC to 0820 UTC with a cold cloud top. However, compared to 0750 UTC, an evident temperature decrease is presented near the cloud core

in the black box at 0820 UTC, corresponding to a descending flow and an in-cloud pressure decrease (Figure 12b).

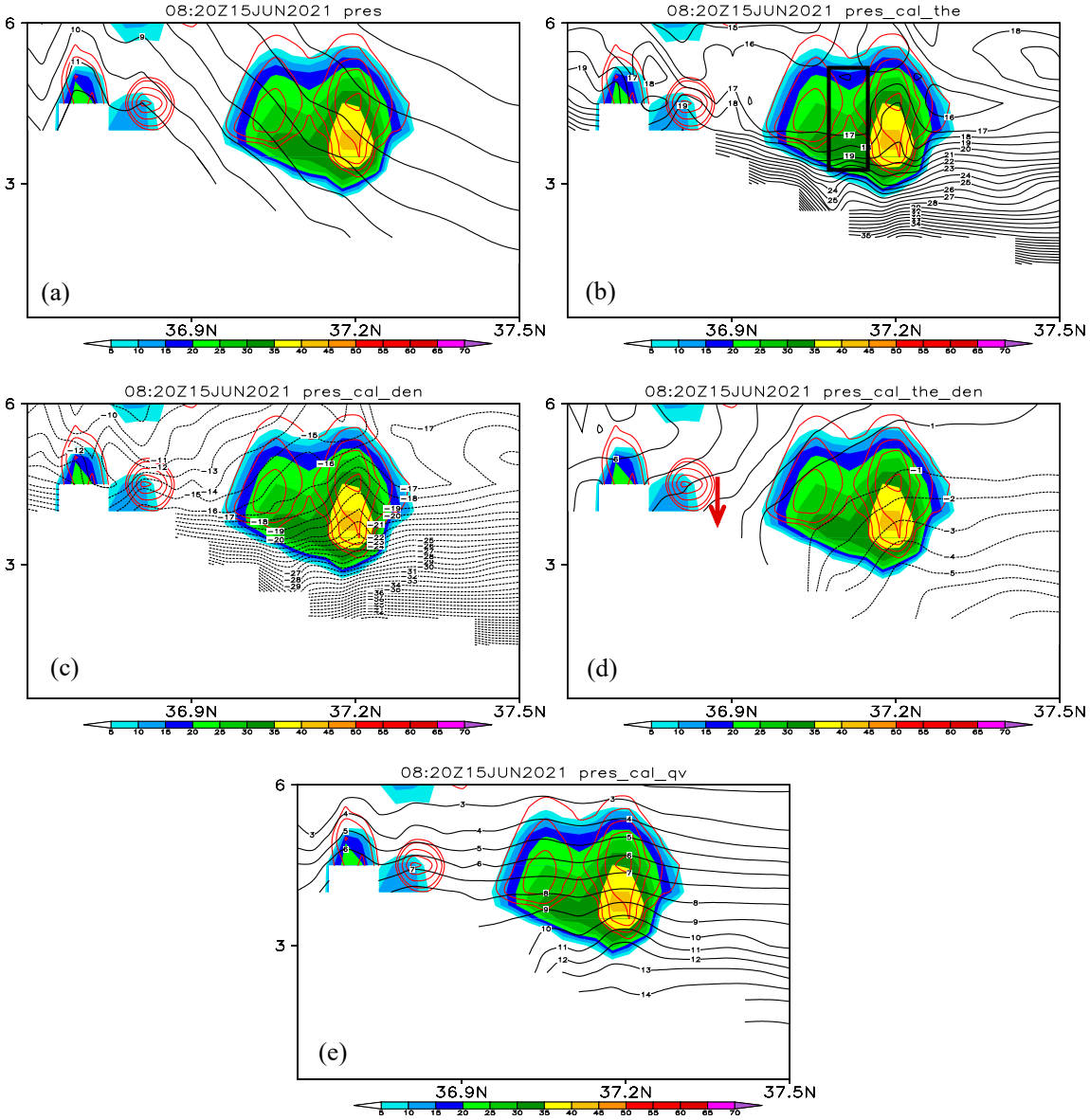

Figure 11. (**a**) Perturbation pressure, (**b**) p'_θ, (**c**) p'_ρ, (**d**) $p'_\rho + p'_\theta$; (**e**) p'_m at 0820 UTC along 78.6° N (contours, unit: hPa). The shaded areas are radar reflectivities. The red contours are the sum of mixing ratios of ice and cloud particles (0.05, 0.1, 0.2, 0.3, 0.4 values, unit: g/kg) to indicate the cloud.

From the vertical distributions of microphysical diabatic heating and divergence along the same section, it is found that the cold temperature perturbation is caused by a mid-level convergence area, which leads a descending of the mid- and upper-level cold, dry air downward into the cloud. The descending appears in the negative Net_WAη areas between two cloud centers, corresponding to a cooling associated with the evaporation and melting. So why does the convergent descending just appear or pass over the developing cumulous? Figure 13 displays the convergence distribution at 7 km height at the several times that are concerned in the paper. In the 7 km height, we found a persistent convergence–divergence dipole in the Tarim Basin, which is northeast–southwest oriented (dotted box). It is interesting that this dipole has existed before the development of the focused cumulous, and the focused convection just appears at the southwest end of the convergence belt, meaning the mid-level convergence has influenced the convection ever since its very initial stage.

It is after 0910 UTC that the mid-level convergence began to separate with the focused convective as the formation of the deep convection. The convergence belt performs as a cap over the cloud. It is difficult to predict when the "cap" can be taken off to make the cloud develop vertically freely.

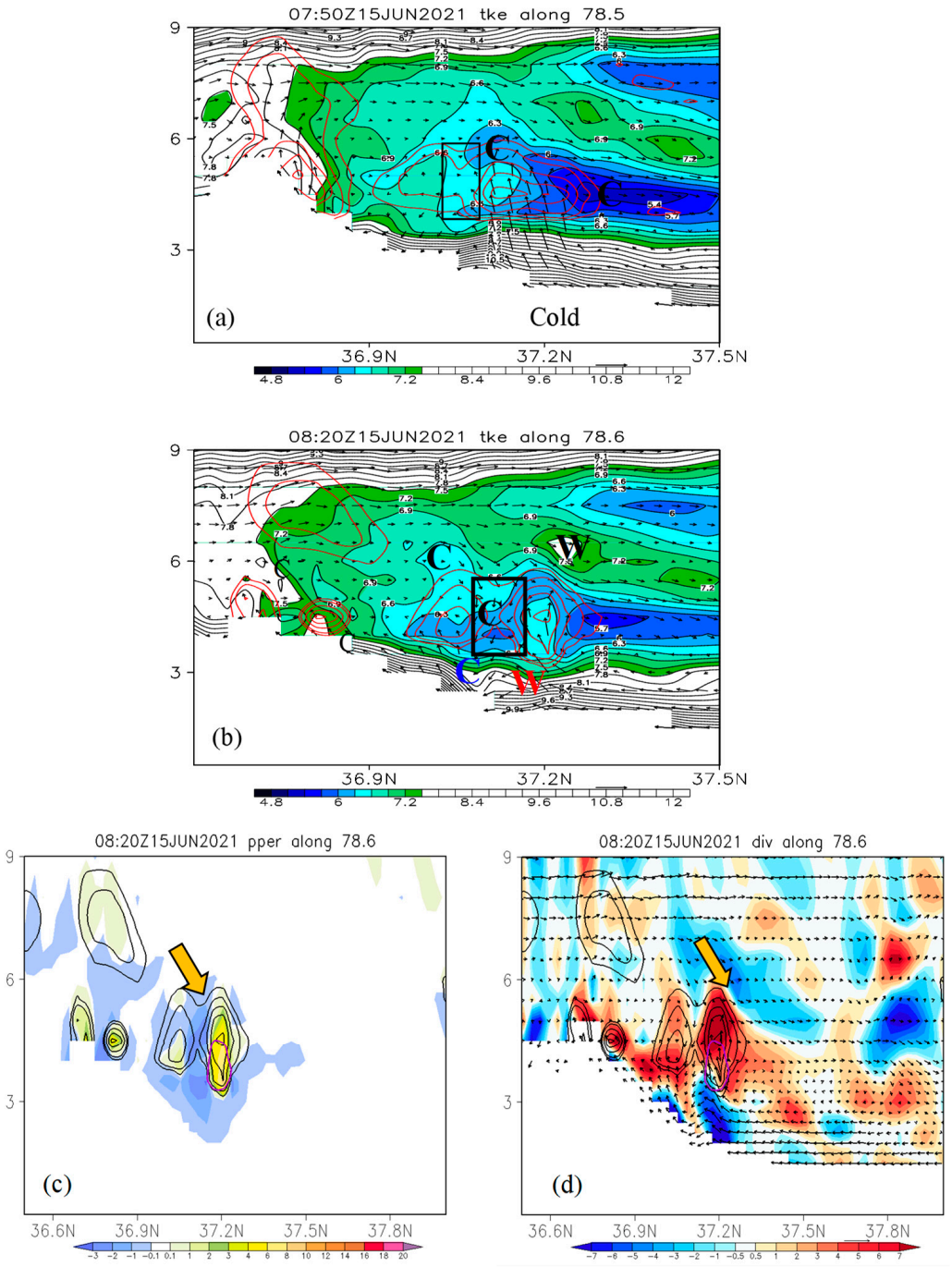

Figure 12. (**a**) Perturbation temperature at 0750 UTC (shaded and contours, unit: K), (**b**) perturbation temperature at 0820 UTC (shaded and contours, unit: K), (**c**) diabatic heating and cooling associated with the microphysical process at 0820 UTC (shaded, unit: 10^{-3} K s^{-1}), (**d**) the 2D divergence field at 0820 UTC (shaded, unit: 10^{-4} s^{-1}) along 78.6° N. The red contours in (**a**,**b**) and black contours in (**c**,**d**) are the sum of mixing ratios of ice and cloud particles (0.05, 0.1, 0.2, 0.3, 0.4 values, unit: g/kg) to indicate the cloud. The vectors are the wind vectors of (v, w) (unit: m/s) in the current section.

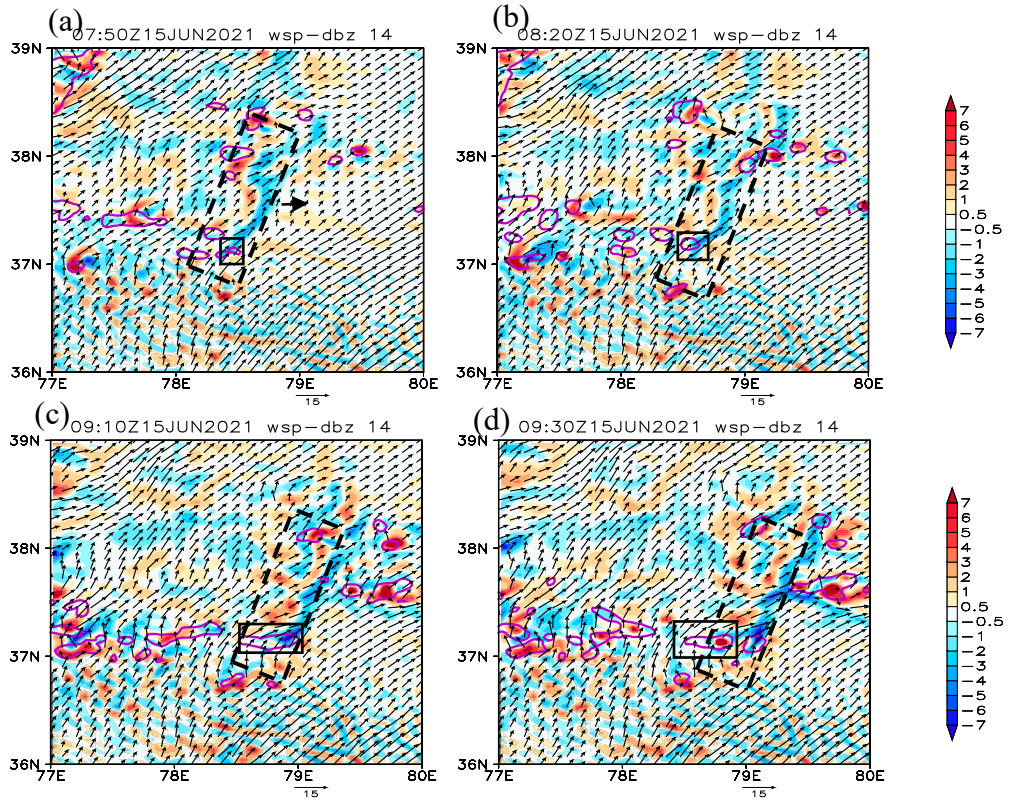

Figure 13. (**a**) The 2D divergence fields (shaded, unit: 10^{-4} s^{-1}) and horizontal wind vectors (arrows, unit: m/s) at 7 km height at 0750 UTC, (**b**) 0820 UTC, (**c**) 0910 UTC and (**d**) 0930 UTC. The purple contours are 35 dBz radar reflectivity.

4.3.3. The In-Cloud Acceleration for Deep Moist Convection Formation

After a nearly two-hour nascent stage, the height of the cloud-top undergoes an evident vertical expansion from 0900 to 1000 UTC, and deep convection is formed. From the above analysis, and from the point view of a typical development picture of deep convection, the CI process needs a large positive Net_WAη in the cloud to take off the "cap" or to break its inhabitation. This condition is just satisfied from 0910 UTC, as shown in Figure 8g–i, in which a strong positive Net_WAη appears both near the cloud top and the low-level area.

Figure 14 presents a comparison of PGF_WRF, B_WRF and their sum at 0850 UTC and 0910 UTC to reveal the mechanism of positive Net_WAη, especially those near the cloud top, which obviously has a main contribution to the following upgrowth of cloud height. In Figure 14a–c, at 0850 UTC, there is still a negative in-cloud Net_WAη because the magnitude of the negative B_WRF is larger than the PGF_WRF. However, 20 min later at 0910 UTC, in Figure 14d–f, the two positive in-cloud Net_WAη centers appear (enclosed by the thick black lines). Meanwhile, a deceleration region characterized by negative Net_WAη develops near the positive region (enclosed by the thick rose red lines). From 0850 to 0910 UTC, PGF_WRF shows an evident increase all over the convective areas with a larger increase in the boundary layers near the cloud base but an evident positive increase center in the cloud top (Figure 14g). On the contrary, the B_WRF presents an opposite change pattern with a larger decrease in the boundary layers and a very small-value center in the cloud top (Figure 14h). From the sum of the PGF_WRF difference and B_WRF difference in Figure 14i, it is easily found that the cloud-top and low-level positive Net_WAη are due to the larger increase in the positive PGF_WRF, and the in-cloud negative Net_WAη is attributed to the negative B_WRF.

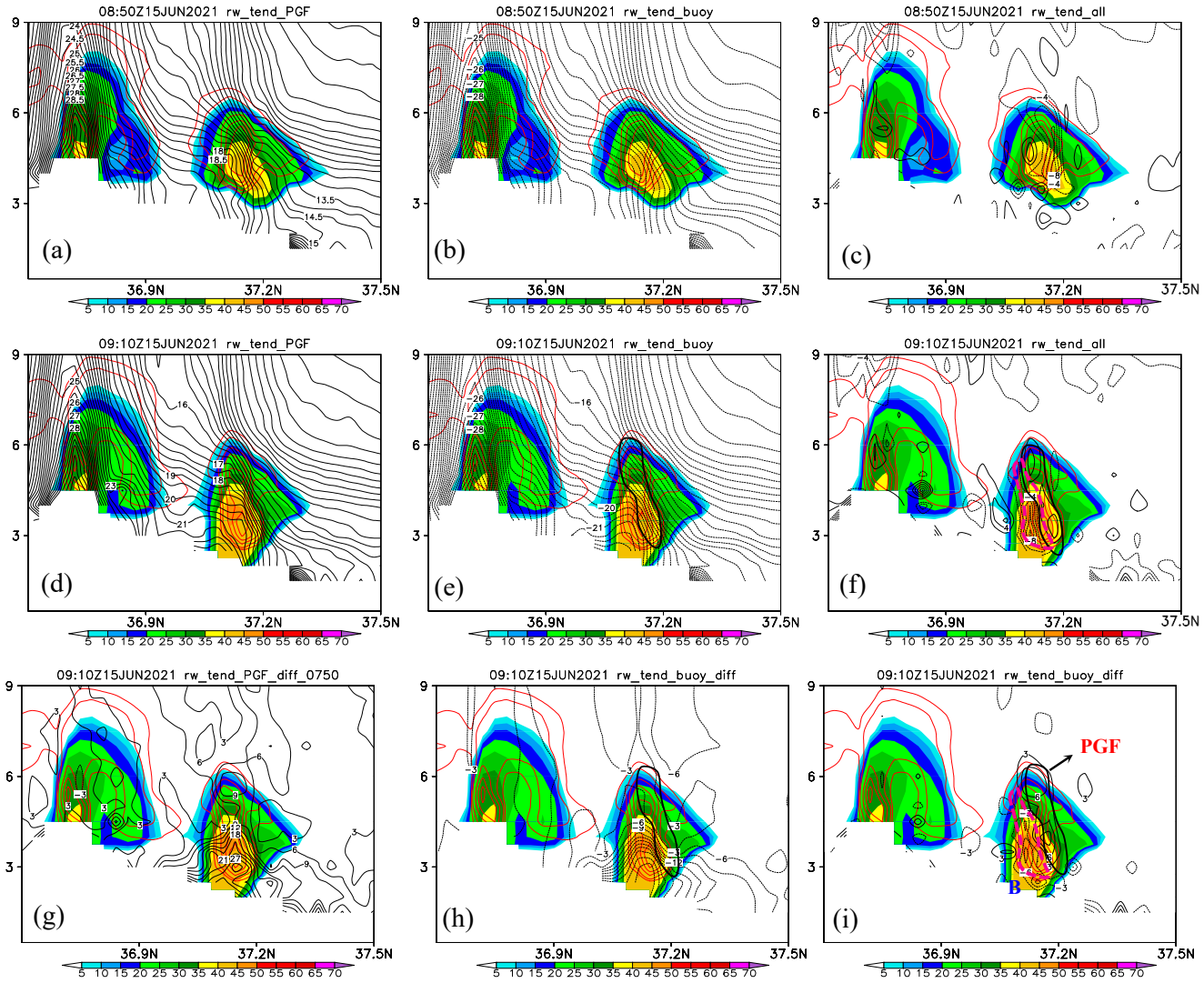

Figure 14. Same as Figure 7 except for the time of 0850 UTC and 0910 UTC. The "difference" means the fields at 0910 UTC minus those at 0850 UTC. The area enclosed by the thick black line is the positive Net_WAη area, while that enclosed by the rose red line is the negative Net_WAη area. "PGF" is the pressure gradient force, and "B" is buoyancy.

Here, we focus on the in-cloud positive Net_WAη due to its most important effect to CI. The difference in the perturbation pressure and its components between 0850 UTC and 0910 UTC along the cloud core are shown in Figure 15. The perturbation pressure presents a whole increase over the cloud area but with two increase centers, respectively, near the cloud base over the surface ground and near the cloud top. The direction of PGF caused by the change in perturbation pressure from 0850 UTC to 0910 UTC is indicated by the red arrows in Figure 15a, which is consistent with the two positive centers of vertical accelerations.

p'_θ (Figure 15b) has an evident increase in the cloud core and a strong decrease in the boundary layer, which is mainly related to the diabatic heating (condensation) and cooling (melting) (Figure 16a,b). The structure of p'_θ is consistent with our general understanding that the diabatic heating due to the moisture condensation or other microphysical processes is a basic process for the formation of DMC, because it makes the convective atmosphere less dense or hotter than the surrounding area. However, from the attitude of the pressure, lighter air means lower pressure. Similar to the previous time, as shown in Figure 15c, p'_ρ mostly presents an opposite pattern to p'_θ. The sum of these two pressures still caused

a downward PGF change both over the cloud top and in the lower levels as shown in Figure 15d. Naturally, the significance of p'_m on the upward PGF_WRF and thus the in-cloud positive Net_WAη is prominent. In Figure 15e, p'_m presents an evident increase in the boundary layer and in the cloud area, displaying a main contribution to the pressure and pressure change in Figure 15a.

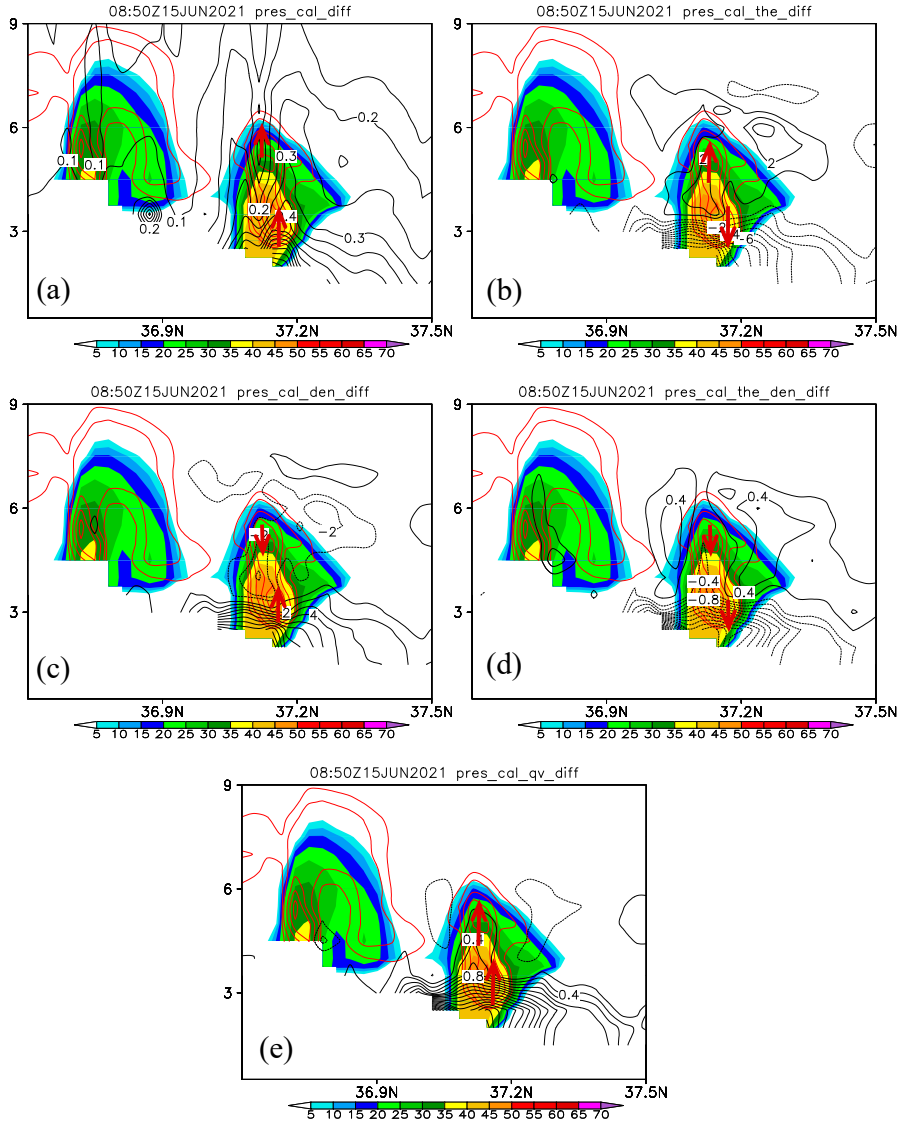

Figure 15. Same as Figure 8 except for the time of 0850 UTC and 0910 UTC. The "difference" means the fields at 0910 UTC minus those at 0850 UTC. The red thick arrows indicate the direction of PGF due to the change in the corresponding perturbation pressure.

Figure 16c,d present distributions of water vapor mixing ratio along the same section as in Figures 14 and 15 at 0850 and 0910 UTC. In Figure 16, one can find an evident increase in moisture in the convective areas in 20 min with a noticeable bulge of q_v contours over the convective atmosphere. The water vapor mixing ratio in the sub-cloud boundary layers increases from 7.2 g/kg at 0850 UTC to 9.0 g/kg at 0910 UTC. It is interesting that this value is consistent with the conventional values of the magnitude of the water vapor mixing ratio for most heavy rainfall cases in north China. Recalling the whole process of CI for the focused convection from 0600 UTC, there is a conveying and gathering of the moisture accompanying the entire CI process, indicating the remarkable role of moisture for the extreme precipitation in dry areas. In addition, the above analysis is also different from the traditional view about CI; it illustrates the reason the moisture must reach a certain amount

to support the development of deep convective clouds. The cloud needs the pressure gradient force caused by the gradient of moisture to provide a positive force to resist the negative force in both the lower levels and cloud-top levels.

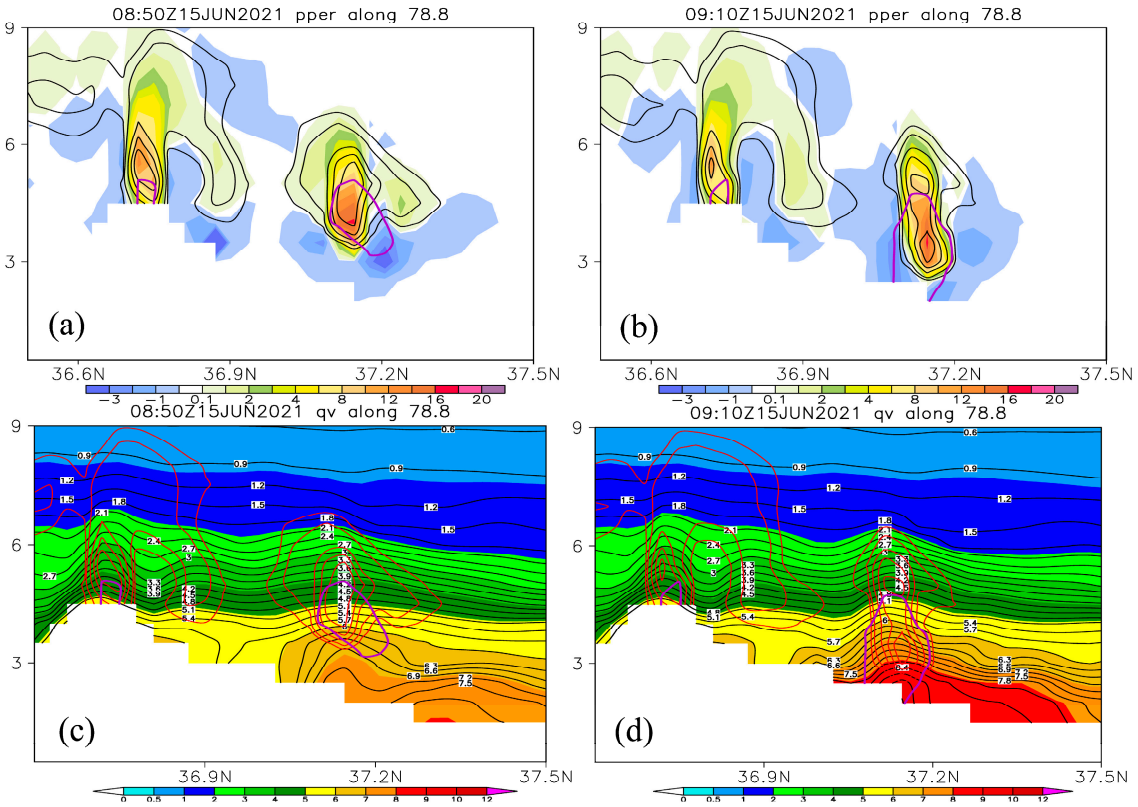

Figure 16. (**a**,**b**) Diabatic heating and cooling associated with the microphysical process (shaded, unit: 10^{-3} K s^{-1}); (**c**,**d**) water vapor mixing ratio (shaded and black contours, unit: g/kg) in the section at 0850 UTC (left column) and 0910 UTC (right column) along 78.8° N. The black contours in (**a**,**b**) and red contours in (**c**,**d**) are the sum of the mixing ratios of ice and cloud particles (0.05, 0.1, 0.2, 0.3, 0.4 values, unit: g/kg) to indicate the cloud. The purple contours are 35 dBz radar reflectivity.

The process associated with the moisture transport and accumulation is shown in Figure 17. In Figure 17a,e, a northwesterly wind blowing toward the Kunlun Mountain appears in the presented area, which was formed by the anticlockwise rotation of the easterly wind in the Tarim Basin as in Figure 2b. The wind was accelerated to about 12 m/s and formed a barrier jet while converging with the northwest-southeast-oriented high terrain. It was evidently shown that the convection has a close relationship with the interaction of the jet and small-scale terrain in which there is convection development or enhancement where the large wind belt reached. The colored tringles indicated four small ridges in Figure 17a. Figure 17e–g present that during the whole initiation process of the focused convection, it strengthened each time it meets the small-scale ridge as indicated in each of the black boxes in Figure 17b–e. Then, after 0930 UTC, the head of the jet separates from the focused jet, but it initiates another convection with the ridge in the purple tringle area. The water vapor corresponding to the jet is shown in Figure 17f–j, which also clearly presents how the moisture front accompanying the jet interests the terrain and accumulates to a small moisture pool due to the small-scale terrain after 0850 UTC at Figure 17i–j. It was approximately from that time that the height of the cloud began to enlarge to form deep convection.

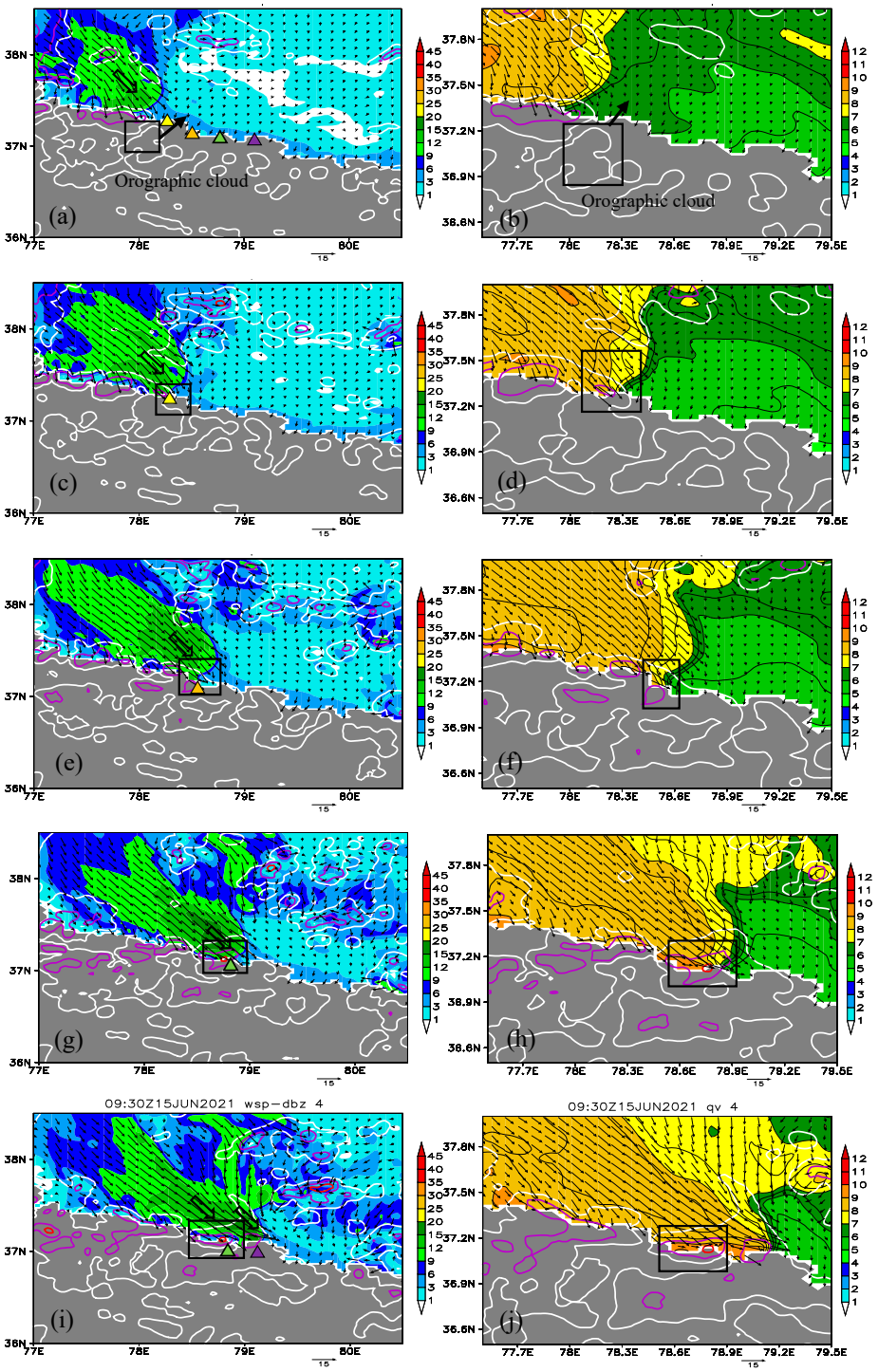

Figure 17. Horizontal wind speed (left column, shaded, unit: m/s) and water vapor mixing ratio (right column, shaded and contours, unit: 10^{-3} g Kg^{-1}) at 2 km height at (**a**,**b**) 0610 UTC, (**c**,**d**) 0700 UTC, (**e**,**f**) 0800 UTC, (**g**,**h**) 0850 UTC, and (**i**,**j**) 0930 UTC. The white, purple and red contours, respectively, represent the 10, 35 and 50 dBz radar reflectivity. The arrows are wind vectors. The black box indicates the location of the focused convection. The colored tringles indicate the small-scale ridges. The thick arrow in (**a**,**b**) indicates the moving direction of the topographic clouds.

5. Conclusions

In the above sections, we gave a detailed analysis on the characteristics of vertical accelerations and the physical processes associated with the accelerations during an extreme-rainfall producing deep convection formation in the most dry areas of China.

Although it is vertical velocity that is responsible for the air transport in the cloud, here we analyze vertical accelerations because a strong vertical velocity for deep convection formation inevitably needs a process of accelerations. Different from the usual criterion for deep convection such as radar reflectivity larger than 35 dBz and mid-level vertical velocity larger than 1 m/s, we focus on the cloud-top height, which is partly because of the very-high terrain in the Kunlun Mountain in southern Xinjiang and the large difficulty of forming deep convection in such dry areas. Also, we hold the view that the lifting of the air passing the free convection level is just a first step in the deep convection formation. When and where the deep convection is formed largely relies on the possible processes it may experience in the cloud.

It is found that the formation of the large-rainfall producing convection cell has three prominent accelerations: the sub-cloud acceleration, the in-cloud deceleration and the cloud-top acceleration. The sub-cloud acceleration was responsible for accelerating the transport of the boundary-layer moist air into the cloud. It may be the very first signal indicating the cloud will go into a rapid development stage. The in-cloud deceleration inhabits the upward development of the convection, which just explains why the unstable air parcel is lifted passing LFC but does not form deep convection. It largely postpones the formation time of deep convection. The cloud-top acceleration contributes to the transition of shallow convection to deep convection by accelerating the vertical motion in the upper part of the cloud.

Different from the previous study which focus on the contributions of the vertical gradient of dynamic perturbation pressure and effective buoyancy (a sum of buoyancy and processes associated with buoyancy vertical gradient) to vertical motions, we directly use the framework of vertical acceleration in the WRF model, finding the key ingredients that promote the deep convection formation in the model. Therefore, although the PGF_WRF and B_WRF are used, they are different from the traditional understanding of PGF and B because they are relative to the initial fields of the model instead of the so-called base-state environment for convection. We use a linear diagnostic relation for perturbation pressure to find the key ingredients. The diagnostic perturbation pressure shows that any change in perturbation pressure is highly determined by the thermodynamic factors such as perturbation potential temperature, specific volume and moisture. It is found that both PGF_WRF and B_WRF contribute to the upward sub-cloud acceleration. They are, respectively, related to an accumulation of moisture in the sub-cloud layer and a three-dimensional divergence. Moisture is not a decisive factor for cloud development because most parts of the low-level jet have high water content. But the upward PGF_WRF associated with moisture offsets the possible negative effects caused by the heating (or cooling) and density change for cloud development in the WRF model. In addition, it is found that three-dimensional divergence in the sub-cloud boundary layer is quite favorable for the rapid development of cloud because it needs a rapid upward transport of moist air out of the sub-cloud layers considering the horizontal convergence in those areas, that is, $\partial w/\partial z > -(\partial u/\partial x + \partial v/\partial y)$.

The in-cloud deceleration is mostly related to a mid-level downward cold air, which is entrained into the cloud and causes the downward change in PGF_WRF due to diabatic cooling. It is found that the downward cold air was due to a mesoscale mid-level convergence area, which has no evident direct relation to the main weather systems of the studied case. However, it does greatly delay the formation of the deep convection by decelerating the vertical motion.

The acceleration pattern during the formation of deep convection is more complex than its nascent stage with both accelerations in the cloud-top and boundary layers and decelerations on the cloud edges. But the cloud-top acceleration shows a central influence which moves the cloud-top upward. It shows that the moisture-related pressure contributes mostly to the cloud-top acceleration, which actually demonstrates the importance of moisture structure to the cloud development in the WRF model. Thus, in the dry areas in southern Xinjiang, once the cyclonically rotated low-level strong wind belts encounters

the small-scale ridges that are favorable for the local rapid concentration of moisture, deep convections obtain evident development.

From the study, we may obtain several tips for the prediction of extreme weather in advance. There are some signals from the very beginning of deep convection development. The most evident is the change in the boundary layer that a positive three-dimensional divergence may activate the rapid upward development of deep cloud. Under a scan of wind-profile radars, this may be observed before convection. The upward air can be decelerated by unexpected high-level cold air, which is a factor that may change the time and location of convection initiation. It may be caused by small-scale processes and is possibly the most difficult factor for CI forecast, because there have not been effective tools to observe and measure the possible mid-level as unfavorable. Then, finally, the zigzag trend of the mountains should be noticed. This small-scale changes of terrains may strengthen the convection by converging the moisture.

Supplementary Materials: The following supporting information can be downloaded at: https://www.mdpi.com/article/10.3390/atmos15121406/s1, Figure S1: Model domain for the simulation superposed by the terrain height (unit: km); Figure S2: The 6-h accumulated precipitation from the CMORPH and WRF simulation: (a,c) 0600-1200 UTC; (b,d) 1200-1800 UTC. The black tringle marked the observed extreme precipitation center of CMORPH; Figure S3: Vertical cross sections of (a) simulated radar reflectivity (shaded, unit: dBz) and vertical velocity (contours, unit: m/s); (b) dw/dt calculated with the left-hand side of Equation (1) in height coordinate, namely $\partial w/\partial t + \mathbf{v}\cdot\nabla w$, in which $\partial w/\partial t$ is calculated with vertical velocity in 10-min interval; (c) WRF output Net_WAη without interpolation to height coordinate; (d) Net_WAη calculated with the right-hand side of Equation (1) using the WRF output fields interpolated to height coordinate; (e) same as (d) but calculated with the right-hand side of Equation (2) with an average over a small-region as the base (34.6–40.6 °N, 76–82.9 °E); (f) Net_WAη calculated with the WRF output fields in η coordinate with the right-hand terms of Equation (3); (g) same as (c) but interpolated into height coordinate. All the units of (b–g) is 10^{-3} s^{-1} and all the pictures are along the cloud core at 78.8° E at 0900 UTC, 15 June 2021. The black contours in (b–g) is mixing ratios of cloud and ice particles (0.05, 0.1, 0.2, 0.3, 0.4 values, unit: g/kg), representing the cloud area. The purple contour in (b–g) is 35-dBz radar reflectivity.

Author Contributions: Methodology, L.R. and W.H.; validation, D.Y., C.Y. and B.J.; formal analysis, N.L. and C.Y.; investigation, L.R.; data curation, P.T. and Q.S.; writing—original draft preparation, N.L.; writing—review and editing, L.R. and C.Y.; visualization, B.J.; supervision, L.R. and D.Y. All authors have read and agreed to the published version of the manuscript.

Funding: This study was supported by the Strategic Priority Research Program of the Chinese Academy of Sciences (Grant No. XDB0760200), Youth Innovation Team of China Meteorological Administration (Grant No. CMA2023QN10), the National Natural Science Foundation of China (Grant Nos. 42475017, U2233218 and 42275010), Beijing Municipal Science and Technology Commission (Grant No. Z221100005222012), the open project of China Meteorological Administration Hydro-Meteorology Key Laboratory (Grant No. 23SWQXM028) and the open project of China Meteorological Administration Key Laboratory of Strong Basin Precipitation (Grant No. 2023BHR-Y18).

Institutional Review Board Statement: Not applicable.

Informed Consent Statement: Not applicable.

Data Availability Statement: The WRF 10-min simulated output is archived at Figshare and the corresponding author can be contacted for access to the data. Due to its proprietary nature, observation data of the precipitation cannot be made openly available but can be requested in http://www.nmic.cn/site/theme.html (accessed on 1 December 2022). Reanalysis data for the weather pattern come from https://cds.climate.copernicus.eu/cdsapp#!/dataset/reanalysis-era5-pressure-levels?Tab=overview (accessed on 1 December 2019). The initial fields of the simulation come from https://www.nco.ncep.noaa.gov/pmb/products/gfs/ (accessed on 1 December 2019).

Acknowledgments: We thank the National Key Scientific and Technological Infrastructure project "Earth System Science Numerical Simulator Facility" for the supportive provision of computing resources.

Conflicts of Interest: The authors declare no conflicts of interest.

References

1. Tan, X.; Shao, D. Precipitation trends and teleconnections identified using quantile regressions over Xinjiang, China. *Int. J. Climatol.* **2017**, *37*, 1510–1525. [CrossRef]
2. Hu, Q.; Zhao, Y.; Huang, A.; Ma, P.; Ming, J. Moisture transport and sources of the extreme precipitation over Northern and Southern Xinjiang in the summer half-year during 1979–2018. *Front. Earth Sci.* **2021**, *9*, 770877. [CrossRef]
3. Zhang, J.; Deng, Z. *An Introduction to Xinjiang Precipitation*; China Meteorological Press: Beijing, China, 1987; 400p.
4. Li, X.; Jiang, F.; Li, L.; Wang, G. Spatial and temporal variability of precipitation concentration index, concentration degree and concentration period in Xinjiang, China. *Int. J. Climatol.* **2011**, *31*, 1679–1693. [CrossRef]
5. Wei, Y.; Gong, M.; Li, H. Spatial-temporal distribution and influence of disastrous rainstorm in Southern Xinjiang during 2010–2019. *J. Arid. Meteorol.* **2021**, *39*, 930–938. [CrossRef]
6. Wang, Y.; Zhou, B.; Qin, D.; Wu, J.; Gao, R.; Song, L. Changes in mean and extreme temperature and precipitation over the arid region of northwestern China: Observations and projection. *Adv. Atmos. Sci.* **2017**, *34*, 289–305. [CrossRef]
7. Donat, M.G.; Angelil, O.; Ukkola, A.M. Intensification of precipitation extremes in the world's humid and water-limited regions. *Environ. Res. Lett.* **2019**, *14*, 065003. [CrossRef]
8. Chen, J.; Zheng, Y.; Zhang, X.; Zhu, P. Distribution and diurnal variation of warm-season short-duration heavy rainfall in relation to the MCSs in China. *Acta Meteorol. Sin.* **2013**, *27*, 868–888. [CrossRef]
9. Yang, X.; Zhou, H.; Zhao, K.; Tang, Z.; Zhao, Y. Variation features of hourly precipitation in Xinjiang province during 1991–2018. *Plateau Meteorol.* **2020**, *39*, 762–773. [CrossRef]
10. Jiao, B.; Ran, L.; Li, S.; Zhou, K. Diagnosis of the Mesoscale Vortex Development Mechanism in a Heavy Rain Event. *Chin. J. Atmos. Sci.* **2022**, *46*, 762–774. [CrossRef]
11. Borque, P.; Varble, A.; Hardin, J. Peak rain rate sensitivity to observed cloud condensation nuclei and turbulence in continental warm shallow clouds during CACTI. *J. Geophys. Res.* **2022**, *127*, e2022JD036864. [CrossRef]
12. Duda, J.D.; Gallus, W.A. The impact of large-scale forcing on skill of simulated convective initiation and upscale evolution with convection-allowing grid spacings in the WRF. *Weather Forecast.* **2013**, *28*, 994–1018. [CrossRef]
13. Kain, J.S.; Coniglio, M.; Correia, J.; Clark, A.J.; Marsh, P.T.; Ziegler, C.L.; Lakshmanan, V.; Miller, S.D.; Dembek, S.R.; Weiss, S.J.; et al. A feasibility study for probabilistic convection initiation forecasts based on explicit numerical guidance. *Bull. Am. Meteorol. Soc.* **2013**, *94*, 1213–1225. [CrossRef]
14. Burghardt, B.J.; Evans, C.; Roebber, P.J. Assessing the predictability of convection initiation in the High Plains using an object-based approach. *Weather Forecast.* **2014**, *29*, 403–418. [CrossRef]
15. Burlingame, B.M.; Evans, C.; Roebber, P.J. The influence of PBL parameterization on the practical predictability of convection initiation during the Mesoscale Predictability Experiment (MPEX). *Weather Forecast.* **2017**, *32*, 1161–1183. [CrossRef]
16. Weckwerth, T.M.; Parsons, D.B. A review of convection initiation and motivation for IHOP_2002. *Mon. Weather Rev.* **2006**, *134*, 5–22. [CrossRef]
17. Markowski, P.; Richardson, Y. *Mesoscale Meteorology in Midlatitudes*; Wiley-Blackwell: Hoboken, NJ, USA, 2010; p. 407.
18. Weckwerth, T.M. The Effect of Small-Scale Moisture Variability on Thunderstorm Initiation. *Mon. Weather Rev.* **2000**, *128*, 4017–4030. [CrossRef]
19. Colbert, M.; Stensrud, D.J.; Markowski, P.M.; Richardson, Y.P. Processes associated with convection initiation in the North American Mesoscale forecast system, Version 3 (NAMv3). *Weather Forecast.* **2019**, *34*, 683–700. [CrossRef]
20. Gasperoni, N.A.; Xue, M.; Palmer, R.D.; Gao, J. Sensitivity of convective initiation prediction to near-surface moisture when assimilating Radar refractivity: Impact tests using OSSEs. *J. Atmos. Ocean. Technol.* **2014**, *30*, 2281–2302. [CrossRef]
21. Lock, N.A.; Houston, A.L. Empirical examination of the factors regulating thunderstorm initiation. *Mon. Weather Rev.* **2014**, *142*, 240–258. [CrossRef]
22. Henderson, D.; Otkin, J.A.; Mecikalski, J.R. Examining the Role of the Land Surface on Convection Using High-Resolution Model Forecasts Over the Southeastern United States. *J. Geophys. Res.* **2022**, *127*, e2022JD036563. [CrossRef]
23. Romps, D.M. A direct measure of entrainment. *J. Atmos. Sci.* **2010**, *67*, 1908–1927. [CrossRef]
24. Kell, C.; Baur, F.; Bachmann, K.; Rasp, S.; Schneider, L.; Barthlott, C. Relative contribution of soil moisture, boundary-layer and microphysical perturbations on convective predictability in different weather regimes. *Q. J. R. Meteorol. Soc.* **2019**, *145*, 3102–3115. [CrossRef]
25. Grant, L.D.; van den Heever, S.C.; Haddad, Z.S.; Bukowski, J.; Marinescu, P.J.; Storer, R.L.; Posselt, D.J.; Stephens, G.L. A linear relationship between vertical velocity and condensation processes in deep convection. *J. Atmos. Sci.* **2022**, *79*, 449–466. [CrossRef]
26. Abulikemu, A.; Xu, X.; Wang, Y.; Ding, J.; Zhang, S.; Shen, W. A modeling study of convection initiation prior to the merger of a sea-breeze front and a gust front. *Atmos. Res.* **2016**, *182*, 10–19. [CrossRef]
27. Abulikemu, A.; Ming, J.; Xu, X.; Zhuge, X.; Wang, Y.; Zhang, Y.; Zhang, S.; Yu, B.; Aireti, M. Mechanisms of Convection Initiation in the Southwestern Xinjiang, Northwest China: A Case Study. *Atmos. Res.* **2020**, *11*, 1335. [CrossRef]
28. Morrison, H. An analytic description of the structure and evolution of growing deep cumulus updrafts. *J. Atmos. Sci.* **2017**, *74*, 809–834. [CrossRef]

29. Peters, J.M.; Morrison, H.; Nowotarski, C.J.; Mulholland, J.P.; Thompson, R.L. A formula for the maximum vertical velocity in supercell updrafts. *J. Atmos. Sci.* **2020**, *77*, 3747–3757. [CrossRef]
30. Grabowski, W.W.; Morrison, H. Supersaturation, buoyancy and deep convection dynamics. *Atmos. Chem. Phys.* **2021**, *21*, 13997–14018. [CrossRef]
31. Peters, J.M.; Morrison, H.; Varble, A.C.; Hannah, W.M.; Giangrande, S.E. Thermal Chains and Entrainment in cumulus updrafts. Part II: Analysis of idealized simulations. *J. Atmos. Sci.* **2020**, *77*, 3661–3681. [CrossRef]
32. Peters, J.M.; Mulholland, J.P.; Chavas, D.R. Generalized lapse rate formulas for use in entraining CAPE calculations. *J. Atmos. Sci.* **2022**, *79*, 815–836. [CrossRef]
33. Powell, S.W. Criticality in the shallow-to-deep transition of simulated tropical marine convection. *J. Atmos. Sci.* **2022**, *79*, 1805–1819. [CrossRef]
34. Rousseau-Rizzi, R.; Kirshbaum, D.J.; Yau, M.K. Initiation of deep convection over an idealized mesoscale convergence line. *J. Atmos. Sci.* **2017**, *74*, 835–853. [CrossRef]
35. Li, N.; Jiao, B.F.; Ran, L.K. On the mechanism of a terrain-influenced snowburst event during midwinter in Northeast China. *Adv. Atmos. Sci.* **2021**, *38*, 800–816. [CrossRef]
36. Kirshbaum, D.J. Large-eddy simulations of convection initiation over heterogeneous, low terrain. *J. Atmos. Sci.* **2022**, *79*, 973–987. [CrossRef]
37. Zhang, Y.H. *Xinjiang Precipitation: 1961–2018*; China Meteorological Press: Beijing, China, 2020; 263p.
38. Wang, Q.; Zhao, Y.; Chen, F.; Yang, Q.; Huang, A. Characteristics of different patterns of South Asia High and their relationships with summer precipitation in Xinjiang. *Plateau Meteorol.* **2017**, *36*, 1209–1220. [CrossRef]
39. Sun, Y.S. The Relation Between Low-Level Jet and Xinjiang Precipitation. Master's Thesis, Nanjing University of Information Science and Technology, Nanjing, China, 2019.
40. Huang, X.; Zhou, Y.; Liu, L. Occurrence and development of an extreme precipitation event in the Ili Valley, Xinjiang, China and analysis of gravity waves. *Atmosphere* **2020**, *11*, 752. [CrossRef]
41. Li, N.; Jiao, B.F.; Ran, L.K. Influence of the upstream terrain on the formation of a cold frontal snowband in Northeast China. *Asia-Pac. J. Atmos. Sci.* **2022**, *58*, 243–264. [CrossRef]
42. Parker, M.D.; Johnson, R.H. Simulated convective lines with leading precipitation. Part I: Governing dynamics. *J. Atmos. Sci.* **2004**, *61*, 1637–1655. [CrossRef]
43. Doswell, C.A.; Markowski, P.M. Is buoyancy a relative quantity. *Mon. Weather Rev.* **2004**, *132*, 853–863. [CrossRef]
44. Xu, X.; Xue, M.; Wang, Y. Mesovortices within the 8 May 2009 bow echo over the Central United States: Analyses of the characteristics and evolution based on doppler radar observations and a high-resolution model simulation. *Mon. Weather Rev.* **2016**, *143*, 2266–2290. [CrossRef]
45. Skamarock, W.C.; Klemp, J.B.; Dudhia, J.; Gill, D.O.; Liu, Z.; Berner, J.; Wang, W.; Powers, J.G.; Duda, M.G.; Barker, D.M.; et al. *A Description of the Advanced Research WRF Model Version 4*; NCAR Technical Note; National Center for Atmospheric Research: Boulder, CO, USA, 2019.